GPS Measurements of Deformation Associated with the 1987 Superstition Hills Earthquake: Evidence for Conjugate Faulting

Shawn Larsen
Seismological Laboratory
California Institute of Technology; Pasadena, CA 91125

Robert Reilinger
Earth Resources Laboratory
Massachusetts Institute of Technology; Cambridge, MA 02139

Helen Neugebauer and William Strange
National Geodetic Survey, NOAA,
Rockville, MD 20852

Abstract

Large station displacements observed from Imperial Valley GPS campaigns are attributed to the November 24, 1987 Superstition Hills earthquake sequence. Thirty sites from a 42 station GPS network established in 1986 have been reoccupied during 1988 and/or 1990. Displacements at three sites within 3 kilometers of the surface rupture approach 0.5 m. Eight additional stations within 20 km of the seismic zone are displaced at least 10 cm. This is the first occurrence of a large earthquake (M_S 6.6) within a preexisting GPS network. Best-fitting uniform slip models of rectangular dislocations in an elastic half-space indicate 130 ± 8 cm right-lateral displacement along the northwest-trending Superstition Hills fault and 30 ± 10 cm left-lateral displacement along the conjugate northeast-trending Elmore Ranch fault. The geodetic moments are 9.4 x 10^{25} dyne-cm and 2.3 x 10^{25} dyne-cm for the Superstition Hills and Elmore Ranch faults, respectively, consistent with teleseismic source parameters. The data also suggest that postseismic slip along the Superstition Hills fault is concentrated at shallow depths. Distributed slip solutions using Singular Value Decomposition indicate near uniform displacement along the Elmore Ranch fault and concentrated slip to the northwest and southeast along the Superstition Hills fault. A significant component of non-seismic secular displacement is observed across the Imperial Valley, which is attributed in part to interseismic plate-boundary deformation.

1. Introduction

The Global Positioning System (GPS) is rapidly becoming one of the most important tools for studying tectonic deformation [e.g., *Larsen*, 1991]. By recording signals from earth orbiting satellites it is possible to determine 3-dimensional coordinates of geodetic monuments with high accuracy [e.g., *King et al.*, 1985; *Wells et al.*, 1987]. The station displacement or deformation between surveys is measured when observations are repeated. GPS can be used to monitor secular deformation such as that associated with plate motion, or to record rapid strain fluctuations such as those due to seismic and volcanic activity. In its final configuration scheduled for the mid 1990's, 21 satellites will be deployed in 6 orbital planes (with 3 additional satellites used as active spares). When GPS becomes fully operational, it will be possible to continuously determine 3-dimensional positions anywhere on or near the earth. The available satellite constellation existing for the last several years was optimized for North America, making geodetic studies in California practical. The observation window in which enough satellites have been visible to obtain the high accuracies necessary to measure tectonic motion has been about 6 to 8 hours each day.

On November 24, 1987, two large earthquakes separated by 12 hours occurred in the northwest portion of the Imperial Valley region of southern California. The first event was located on a northeast-trending seismic lineament and was followed 12 hours by rupture along the northwest-trending Superstition hills fault. What makes this earthquake sequence so significant from a GPS standpoint, is that it occurred spatially and temporally within a preexisting GPS network. This network was established in the Imperial Valley in 1986, with partial resurveys in 1988 and 1990. Fifteen stations are located within 20 km of the rupture zone; three stations are within 3 km. This is the first occurrence of a large earthquake within a preexisting GPS network.

We compute GPS displacements in the Imperial Valley between 1986 and 1990. Observed station movements of nearly 0.5 meters are attributed to the Superstition Hills earthquake sequence. The earthquake-induced displacements are inverted to estimate seismic slip and the geodetic moment along the rupture planes. In addition, there is a large component of deformation which can not be explained by the seismic disturbance. We assume this to be, in part, a manifestation of continuous strain accumulation across the Imperial Valley due to the relative motion of the Pacific and North American plates.

2. Imperial Valley Seismicity and Tectonics

The Imperial Valley region of southern California is a complex transition zone between crustal spreading in the Gulf of California and right-lateral transform motion along the San Andreas fault (Figure 1) [*Lomnitz et al.*, 1970; *Elders et al.*, 1972]. The valley is 4 - 12 million years old and has been filled by up to 15 km of late Cenozoic sediments [*Larson et al.*, 1968; *Moore and Buffington*, 1968; *Ingle*, 1974; *Fuis et al.*, 1982]. The major fault systems and structural grain of the valley trend to the northwest, roughly parallel to the direction of plate motion. A significant fraction of the North American and Pacific relative motion may be accommodated across this region.

The Imperial Valley is one of the most seismically active regions of California (Figure 1). Much of this activity occurs along the Imperial fault and within the Brawley Seismic Zone [*Johnson and Hill*, 1982]. Several large earthquakes have occurred in and near the Imperial Valley since 1940 (Figure 1). The Imperial fault ruptured with a M_S 7.1 event in 1940 and a M_L 6.6 event in 1979 [*U.S. Geol. Surv.*, 1982]. Segments of the San Jacinto fault system broke with a M_L 6.2 earthquake in 1954 and a M_L 6.5 event in 1968 (Borrego Mountain). The most GPS relevant episode of seismic activity occurred in 1987 along the Superstition Hills segment of the San Jacinto fault system, with a M_S 6.2

earthquake on a northeast-trending seismic lineament followed 12 hours by a M_S 6.6 event on the Superstition Hills fault.

Conventional geodetic measurements suggest considerable deformation across the Imperial Valley. In fact, a significant fraction of the Pacific-North American relative plate motion may be accommodated here. New global plate model estimates (NUVEL-1) [*DeMets et al.*, 1987; *DeMets et al.*, 1990] predict the rate of motion between the North American and Pacific plates (at Imperial Valley coordinates: 33.0°N, 115.5°W) is 4.7 cm/yr oriented N39.6°W. Triangulation measurements spanning this region suggest 4.3 cm/yr of plate-boundary deformation averaged between 1941 and 1986 [*Snay and Drew*, 1988]. Trilateration measurements made by the U.S.G.S. between 1972 and 1987 indicate 3.45 cm/yr relative movement between stations on opposite sides of the valley [*Prescott et al.*, 1987b]. The orientations of the conventional geodetic displacements are approximately N40°W, although to some extent the direction is non-unique and depends upon a priori assumptions [e.g., *Prescott*, 1981]. In addition, the conventional geodetic measurements indicate that deformation is concentrated in a narrow 20 km wide zone along the Imperial fault, while to the north it is distributed over a region at least 50 km wide. Presumably, deformation is transferred from the Imperial fault, which acts as the primary strain release mechanism near the border, to distributed shear along the San Andreas, San Jacinto, and Elsinore faults.

3. Superstition Hills Earthquake Sequence

On November 24, 1987 (1:54 GMT), a M_S 6.2 earthquake occurred along a northeast-trending seismic lineament northeast of the Superstition Hills fault (Figure 2) [*Magistrale et al.*, 1988]. The focal mechanism and aftershock sequence, which extended for 26 km into the Brawley Seismic Zone, are consistent with left-lateral strike slip

motion on a vertical fault. Seven foreshocks were recorded in the 22 minutes prior to the main event, including two with $M_L > 4.0$. Surface rupture consisted of a complex pattern of left-lateral northeast-trending offsets ranging in length from 1.5 to 10 km, and with maximum displacements between 3 and 13 cm [*Budding and Sharp*, 1988; *Hudnut et al.*, 1989a]. We refer to this northeast-trending lineament as the Elmore Ranch fault, although more precisely this name refers only to the longest of the surface fractures.

Twelve hours after the Elmore Ranch event (13:15 GMT), a M_S 6.6 earthquake occurred along the northwest-trending Superstition Hills fault. The epicenter was near the intersection of the Elmore Ranch and Superstition Hills faults. Strong ground motion and teleseismic data suggest the rupture process for this second event was somewhat complicated, consisting of multiple sub-events [*Bent et al.*, 1989; *Frankel and Wennerberg*, 1989; *Hwang et al.*, 1990; *Wald et al.*, 1990]. Surface rupture extended 24 km along the previously mapped trace of the fault [*Williams and Magistrale*, 1989]. Up to 50 cm right-lateral displacement were measured immediately following the earthquake. The aftershock pattern was concentrated slightly to the west of the fault and did not extend the length of the surface rupture. *Magistrale et al.* [1989] suggested the aftershock sequence was highly correlated with basement structure. Both the Superstition Hills and Elmore Ranch events triggered sympathetic surface offsets along the Imperial, San Andreas, and Coyote Creek faults [*McGill et al.*, 1989; *Hudnut and Clark*, 1989].

Significant afterslip was recorded along the Superstition Hills fault following the second mainshock [*Williams and Magistrale*, 1989]. No afterslip was measured along any of the surface ruptures associated with the Elmore Ranch event. In fact, all seismic activity essentially stopped along this segment after the initiation of the 2nd mainshock.

One of the most interesting aspects of this earthquake sequence is the conjugate nature of faulting. That is, two surface ruptures oriented nearly perpendicular to each

other. As discussed below, this type of fault interaction may be typical of Imperial Valley tectonics and may dictate the mode of stress/strain transfer from one fault system to another.

What makes the Superstition Hills earthquake sequence unique from a GPS perspective is that it occurred within a preexisting GPS network. Stations located near the seismic rupture zone were displaced nearly 0.5 meters. These movements, as well as smaller displacements observed at nearby stations, can be inverted to infer properties of the rupture process. This is the first time GPS measurements have recorded the deformation from a large earthquake.

4. GPS Observations

The signal structure broadcast from each GPS satellite consists of two carrier phase signals modulated by a navigational message and pseudo-random codes. The two carrier frequencies, known as the L1 and L2 phases, are broadcast at 1575.42 Mhz (L1) and 1227.60 Mhz (L2). This is equivalent to wavelengths of about 19 cm for the L1 and 24 cm for the L2. The navigational message contains the satellite coordinates (broadcast ephemeris), clock parameters, satellite health, and general system status. The pseudo-random codes are accurate time marks which allow a GPS receiver to determine the transmission time of the signal. When scaled by the speed of light, the pseudorange, or the time-biased satellite-receiver distance is computed. If measurements to at least 4 GPS satellites are available, and if the satellite coordinates are known (usually with the broadcast ephemeris), the 3-dimensional receiver position and the satellite-receiver time offset can be determined. The positioning accuracy with the pseudorange is 1 to 100 m, depending on whether the P or C/A code is used, the receiver type, length of observation, and the static or kinematic behavior of the instrument. It is the

pseudorange which will be used for civilian and military navigation. For highly accurate geodetic positioning, however, it is necessary to use the carrier phase measurements in a post-processing mode. That is, the data collected in the field are brought back to the office or laboratory for analysis, usually with a fairly robust computer software system. More complete details about the Global Positioning System, including theoretical aspects and processing methods, are found in *King et al.* [1985], *Wells et al.* [1987], and *Rocken* [1988].

GPS Surveys -- Data Collection

The GPS data for this study were collected during 4 Imperial Valley field campaigns from 1986 to 1990 (Table 1). A total of 46 stations in or near the valley have been occupied at least once during this interval, while 30 sites have been reoccupied since 1986 (Figure 3). TI-4100 GPS receivers supporting GESAR software were used during 1986 and 1988, while Trimble 4000SST instruments were used during the 1990 survey. A comprehensive discussion regarding the data collection methods is given in *Larsen* [1991].

The National Geodetic Survey (NGS) occupied 54 sites in southern California in May/June 1986; 42 stations were located in or near the Imperial Valley. Most marks were observed at least two days, although redundant baselines were relatively uncommon (i.e., simultaneous occupation of the same station-station pair for two or more days). This was one of the first GPS networks established to investigate crustal motions. In fact, GPS surveying at this time was still at an "experimental stage." The scheduled 4.5 hour daily occupations were somewhat less than the 6-8 hour sessions typical of more recent southern California campaigns. There was less than a 2 hour period each day in which more than 3 satellites were simultaneously tracked, and there was a scheduled 1 hour gap in Satellite 6 during the middle of the measurement session. In addition, due to a variety of equipment and logistical problems, less than 2 hours of data were

collected at several sites. The data were generally noisy and processing was unusually tedious. The final double difference phase observables may contain uncorrected cycle slips. Because of these unfortunate circumstances due to the earliness of this survey, the quality of the data is fairly poor.

In February/March 1988 university field crews (UNAVCO) observing for 9 days reoccupied 15 of the Imperial Valley marks, as well as establishing 4 new stations along the Salton Sea. These new sites were installed at tide gauge monitoring facilities and will be used to constrain vertical GPS baseline components and for monitoring tectonic tilting in the Salton Trough. Most monuments were occupied for 2 days (1 was observed 3 days, 1 for 4 days, and 2 for 1 day). The scheduled nightly observation scenario lasted 7.5 hours, with a total of 7 satellites tracked.

In March/April 1988 the NGS reoccupied 21 of the 1986 stations (7 of which were observed by the university crews a month earlier). Most sites were occupied only 1 day. The daily observation period of 6.0 hours was slightly shorter than the February/March survey, although 7 satellites were tracked each day.

In addition to the UNAVCO and NGS campaigns, GPS observations in 1988 were made at Mojave (California), Westford (Massachusetts), and Richmond (Florida). These sites are continuously monitored as part of the Cooperative International GPS Network (CIGNET) [*Chin*, 1988]. Data from CIGNET stations are used to improve satellite orbits in the GPS processing. Unfortunately, these observations are frequently of poor quality and contain abundant cycle slips. During the 1988 campaign, observations were not always available or usable at all CIGNET sites on all days [*Larsen*, 1991].

Station MOUN (Mound), which was surveyed in 1986, was destroyed from the 1987 earthquake sequence. The site is located less than 1 km from the surface rupture of the

Superstition Hills fault. Field investigation during early 1988 reveiled that the monument and supporting concrete base had been completely uprooted from the ground. Destroyed monuments usually can not be tied to previous surveys because of the high accuracy required for crustal motion research. If the suspected deformation is significantly large, however, some information may be recovered if the monument (or a substitute) is reset in approximately the same location. Site inspection at MOUN clearly showed the position of the old monument and in early April, 1990, a rebar rod acting as a temporary benchmark was set at approximately the same location. We estimate the temporary mark was set within 0.15 m of the previous monument. Because of its proximity to the 1987 rupture zone, the calculated seismic displacement at MOUN is about 0.5 m. Therefore, reoccupation of this site should retrieve a tectonic component larger than the expected uncertainty.

The 1990 survey was conducted to establish the displacement of MOUN relative to its 1986 position. This "mini-campaign" included stationary GPS receivers at only three sites (Table 1). It was performed interactively with kinematic GPS transects along the southern San Andreas fault. Data were collected for only one night; a total of 9 satellites were visible during the scheduled 7.0 hour experiment.

GPS Processing

The 1986 GPS observations were processed with the GPS22 software developed at the National Geodetic Survey. Satellite orbital information was provided by the NSWC (Naval Surface Weapons Center). A tropospheric delay parameter was solved at each station, constrained by surface meteorological measurements. Ambiguities were fixed to the nearest integer. Each of the 20 days of observation was processed separately, and the daily solutions were combined to form one set of station coordinates with the geodetic adjustment program DYNAP (DYNamic Adjustment Program) [*Drew and Snay,*

1989]. All coordinates were computed in the WGS-84 reference frame [*Defense Mapping Agency*, 1987]. Due to the relatively poor data quality, the accuracy of these measurements is believed to be on the order of 1 ppm (parts per million).

Data from both 1988 campaigns were processed with the Bernese GPS analysis software (version 3.0), from the University of Bern in Switzerland. (Preliminary processing such as data translation and cycle slip fixing were performed with an earlier version of the software.) The Bernese GPS package allows 3-dimensional station coordinates to be determined from the integration of carrier phase, pseudo-range, and orbital data [e.g., *Gurtner et al.*, 1985; *Beutler et al.*, 1985; *Rocken*, 1988]. In addition to measuring station coordinates, the double difference estimation algorithm can solve for adjustments to six Keplerian elements and two radiation pressure coefficients for each satellite, an atmospheric zenith delay parameter at each station, a clock error term at each site, ionospheric model coefficients, and cycle ambiguity terms [e.g., *Rocken*, 1988].

For each of the 1988 surveys, all data were combined into a simultaneous multi-day solution. Surface meteorologic data (temperature, pressure, relative humidity) were used to constrain a Saasmotonian atmospheric model, and independent tropospheric zenith delay parameters were estimated at each station. We experimented with fixing ambiguities but found mixed results, therefore, ambiguities were left unresolved in the final analysis.

In addition to station coordinates, satellite orbital parameters were estimated for both solutions. GPS observations from the CIGNET tracking sites were used to constrain the orbits. The Bernese software is able to combine ephemeris information from several days into a single multi-day arc. It has been suggested that multi-day satellite arcs significantly improve GPS precision [e.g., *Lichten*, 1987]. Typically, 6 Keplerian elements and 2 radiation pressure coefficients are estimated for each satellite.

Davis et al. [1989] utilized 4-day arcs (72 hours plus the length of the daily observation session) to analyze GPS data from North America. A 5-day satellite arc was used to process GPS data off the southern California coast near Santa Barbara [*Larsen et al.*, 1991].

There comes a point, however, when the force model describing the satellite orbits begins to break down. It is unlikely that the 10-day interval of the February/March 1988 survey (9 observation days plus one day of no measurements) could be modeled from a 10-day satellite arc. For purposes of orbit determination, therefore, this campaign was divided into multiple 3-day arc segments (Julian days 55-57, 58-60, and 62-64), each defined by its own initial conditions. The data were still processed simultaneously, except that independent satellite parameters were estimated for each 3-day arc. For the entire campaign, 18 Keplerian orbital elements and six radiation pressure terms were estimated for each satellite. A similar technique was used for the March/April survey. The satellite orbits for this campaign were defined by two 3-day arcs (Julian days 88-90 and 91-93).

Orbits were improved by holding the coordinates of at least 3 CIGNET stations fixed, to values well determined from VLBI and satellite laser ranging [Murray and King, MIT interoffice memorandum, 1988]. The GPS phase observables from these fiducial sites constrain the orbits, which in turn improve solution accuracy of the which in turn improve solution accuracy of the unfixed stations. There was always at least one day in each 3-day arc interval where observations from 3 fiducial sites were available [*Larsen*, 1991].

After each 1988 campaign was processed separately, the Cartesian coordinate differences from the two solutions were adjusted by least squares to obtain one set of coordinates for that year.

The 1990 "mini-campaign" was processed with the Trimvec software, made available from the receiver manufacturer (Trimble Navigation, Sunnyvale, California). Recall that the purpose of this survey was to establish the displacement at station MOUN, presumed large because of its proximity to the 1987 seismic rupture. Since this mark had been reset between the 1986 and 1990 occupations, the error in the displacement estimate will be fairly large (~ 15 cm). Therefore, high accuracy from a GPS perspective was not required. The orbits were given by the broadcast ephemeris, and surface meteorological data were used to constrain a tropospheric delay model.

Station Displacements 1986-1988

GPS station displacements for the interval 1986 to 1988 are shown in Figure 4. All movements are made relative to station OCTI. Only the horizontal components are shown. The method in which errors are formulated and utilized is disussed below. Generally, the observed displacements can be decomposed into 3 components: 1) seismic deformation due to the Superstition Hills earthquake sequence, 2) secular deformation due to the Pacific-North American relative plate motion, and 3) unusually large measurement error, most apparent in the east-trending direction.

The GPS displacement vectors suggest considerable deformation between the 1986 and 1988 campaigns, of which a significant fraction is attributed to the 1987 Superstition Hills earthquake sequence. Stations nearest the seismic rupture zone (KANE and L589) show movements on the order of 40 cm. In fact, the 13 km KANE-L589 baseline was shortened by 70 cm. The orientations of the displacements are consistent with the conjugate fault pattern indicated by the mapped surface offsets (i.e., right-lateral rupture on the Superstition Hills fault and left-lateral rupture along the Elmore Ranch fault). Other stations near the active fault system appear to have been affected by the 1987 event.

There is an additional component of displacement not readily explained by the seismic deformation. Stations east of the Imperial fault tend to be moving south or southeast relative to sites on the other side of the valley. This secular displacement is attributed to the relative motion between the North American and Pacific plates. Unfortunately, it is difficult to ascertain the magnitude of this deformation since station coverage west of the Imperial fault is somewhat lacking and many of these sites have rather large seismically induced displacements (recall that all GPS vectors are relative to OCTI). However, the deformation does appear to be considerable, which is not too surprising considering conventional geodesy indicates a significant fraction of the relative plate motion is occurring across the Imperial Valley.

Also evident in Figure 4 are unusual movements which do not appear to be tectonically related. Most notable are the southwest-trending vectors (as opposed to southeast) for those sites near the border east of the Imperial fault. It appears as if the entire network has undergone a systematic clockwise rotation. We have investigated this possibility by assuming the network could be rotated (and translated) in terms of an outer coordinate solution by minimizing the displacement component perpendicular to the structural axis of the valley (N40°W) [e.g., *Prescott*, 1981]. Stations KANE and L589 were not included in the solution. However, the applied adjustment did not correct for the anomalous displacements, and in fact, made the apparent deformation less uniform. Although these unusual movements can not be attributed to a simple coordinate rotation, they can be explained by large east-trending systematic errors in the 1986 data. This is consistent with the longitudinal orientation of the computed error ellipses (see below), and suggests the north-trending displacement components may be a more reliable indicator of tectonic deformation.

Station Displacements 1986-1990

The 1986-1990 displacement of MOUN relative to BLAC is shown in Figure 5 (dashed arrow). Although the uncertainty is large because MOUN was reset between surveys, the GPS data indicate significant movement attributed to the Superstition Hills events (recall MOUN is less than 1 km from the 1987 surface rupture). However, based on conventional geodesy as well as the 1986-1988 GPS movements, a non-seismic displacement component is suspected in the measurement. We attempt to remove this component by estimating the MOUN-BLAC secular displacement based on EDM observations. This is discussed in more detail below. We remove 2 years of the accumulated MOUN-BLAC secular movement, and then compute the displacement relative to station OCTI. Although the measurement still contains 2 years of non-seismic deformation, it places the displacement into the same reference frame as the 1986-1988 movements. The adjusted MOUN displacement is shown in Figure 5 (solid arrow).

Station Displacements 1988-1988 (February-April)

Seven GPS sites were occupied during both 1988 campaigns; calculated site displacements for this 1 month interval are shown in Figure 6. An adjustment (simple translation) was applied to all movements so that the sum of the vector displacements is zero. The magnitude of the apparent movements range from 0.9 to 2.9 cm, averaging 1.6 cm. It is interesting that the 2.9 cm displacement at KANE is to the west-southwest. This would be expected if left-lateral afterslip occurred along the Elmore Ranch fault. However, while postseismic offsets were significant along the Superstition Hills fault, almost all Elmore Ranch activity ceased after the initiation of the 2nd main event [*Williams and Magistrale*, 1989; *Magistrale*, 1989; *Hudnut et al.*, 1989a]. The observed displacements in Figure 6 probably represent measurement error and not real deformation. Note that the largest vector components are oriented along the longitudinal

direction. Station O217 also exhibits a fairly large apparent east-trending movement, although this is almost certainly not tectonically related.

Even if the displacements shown in Figure 6 are entirely measurement error, they do illustrate two points: 1) GPS accuracy is easily sufficient to monitor tectonic motions, and 2) the anomalous displacements for the 1986-1988 interval (Figure 4) are probably due to the quality of the 1986 data. Typical crustal deformation rates across major tectonic structures in southern California are between 1 and 5 cm/yr. At 1 to 2 cm GPS accuracy, such deformation might be resolvable in as short as 1 year. Although the short baseline ($\sim$ 50 km) horizontal precisions computed from GPS repeatability studies are generally at the sub-centimeter level [e.g., *Dong and Bock*, 1989], these tests usually involve multiple occupations of the same network over a consecutive 4 to 5 day interval. The 7 stations shown in Figure 6 were not all observed simultaneously [*Larsen*, 1991]. Therefore, the repeatability is somewhat degraded since errors tend to propagate through the solutions. However, the relatively good consistency suggested with the 1988 results suggest that some of the unusual movements observed with the 1986-1988 displacement vectors are probably due to the quality of the 1986 data.

GPS Errors

Formal estimates of GPS uncertainty almost always underestimate variances derived from repeatability studies. We attempt to determine more realistic and illustrative errors by multiplying the formal covariance matrix calculated with each GPS solution by an estimated variance factor, which scales as the average baseline length. We have chosen a variance factor for the 1986 data so that the average baseline error scales as 1 ppm. Since the 1988 data were processed robustly utilizing orbit improvement techniques (not available with the 1986 data), we assume these errors are negligible. Although this method is somewhat ad hoc, it does illustrate an important fundamental.

Notably, the east-trending error is about 4 times larger than the north-trending error. This is attributed to the north-south ground-track of the satellite orbits.

Because station MOUN was reset between the 1986 and 1990 surveys, the largest error source is due to the difficulty in establishing the new mark at the previous location. From field inspection, this uncertainty is estimated to be 15 cm (in all directions) and is additive to the GPS measurement error.

5. Modeling

Theory

Simple dislocation theory is often used to model seismically induced geodetic deformation. The earth is considered a homogeneous isotropic elastic half-space with no stress applied to the free surface. The displacement field u_k for a dislocation Σ in the medium is given by

$$u_k = \frac{1}{8\pi\mu}\int\int_{\Sigma} \nabla u_i w_{ij}^k v_j d\Sigma \qquad (1)$$

where ∇u_i is the discontinuity, w_{ij}^k are the displacement Green's functions due to a set of strain nuclei, and v_j are the direction cosines of the normal to the surface element $d\Sigma$ [*Steketee*, 1958; *Chinnery*, 1961]. Analytical solutions to this integral are rather complex, but have been simplified for special cases of dislocation or fault geometry [e.g., *Chinnery*, 1961; *Savage and Hastie*, 1966; *Mansinha and Smylie*, 1967]. General expressions of the displacement field for rectangular strike and dip-slip faults of arbitrary inclination have been computed by *Mansinha and Smylie* [1971] and *Okada* [1985]. Arbitrary slip directions can be designed by the superposition of strike and dip-slip dislocations.

The strain/stress within a medium is computed by differentiating the displacement field. For the displacement u_k, where u is a function of the geometrical coordinates x_i,

the strain tensor components are given by

$$\epsilon_{ij} = \frac{1}{2}\left(\frac{\partial u_i}{\partial x_j} + \frac{\partial u_j}{\partial x_i}\right) \tag{2}$$

In an isotropic medium the stress tensor σ is given by

$$\sigma_{ij} = \lambda\theta\delta_{ij} + 2\mu\epsilon_{ij} \tag{3}$$

where θ is the dilatation ($\theta = \sum_{i=1}^{3}\epsilon_{ii}$). We assume the medium is a Poisson solid with $\lambda = \mu = 2.8\text{x}10^{11}$ dyne-cm^{-2}.

A rectangular dislocation within an elastic half-space will create a spatially dependent stress tensor σ throughout the volume. The force acting at a point along an arbitrarily oriented plane in the medium is computed by multiplying σ by the outward normal vector to the plane ($\vec{N}_n$). That is, the traction vector $\vec{T}$ is given by

$$\vec{T} = \sigma\vec{N}_n \tag{4}$$

If we assume the plane is coincident with a fault, then the forces generated on this secondary structure due to the initial dislocation are determined by calculating the traction vectors at selected points along the fault. The normal (σ_n), strike-slip (σ_s), and dip-slip (σ_d) stresses on the fault plane are computed by

$$\sigma_n = \vec{T}\cdot\vec{N}_n \tag{5a}$$

$$\sigma_s = \vec{T}\cdot\vec{N}_s \tag{5b}$$

$$\sigma_d = \vec{T}\cdot\vec{N}_d \tag{5c}$$

where $\vec{N}_n$, $\vec{N}_s$, and $\vec{N}_d$ are the normal vectors perpendicular, along strike, and along dip to the fault plane. Analytic solutions for the stress and strain fields due to a dislocation within a medium are given by *Iwasaki and Sato* [1979] and *Alewine* [1974].

Inverse Methods

Inversion of seismically generated geodetic displacements can yield fault-rupture

parameters, such as the slip distribution along a fault plane [e.g., *Ward and Barrientos*, 1986; *Harris and Segall*, 1987; *Segall and Harris*, 1987; *Snay*, 1989]. We employ a method similar to that outlined in *Segall and Harris* [1987]. Singular Value Decomposition (SVD) [e.g., *Lanczos*, 1961; *Jackson*, 1972; *Menke*, 1984] and elastic dislocation theory are used to invert the Imperial Valley GPS measurements for seismic slip along the Superstition Hills and Elmore Ranch faults.

The relationship between surface deformation and slip along a rectangular dislocation is defined by Equation (1). The rupture plane is modeled as a set of non-overlapping rectangular dislocations. That is, the fault plane is partitioned into multiple sub-elements or sub-faults. The slip distribution along the seismically active fault is given as the discreate approximation of slip along each sub-element. The normal equations which govern surface displacement resulting from such slip is given by

$$\mathbf{A}^g \mathbf{m}^f = \mathbf{d}^g \tag{6}$$

where the superscripts g and f refer to geodetic observation and fault slip, respectively. Each row of $\mathbf{A}^g$ is determined from (1), and is a function of sub-fault geometry and geodetic position. The slip distribution $\mathbf{m}^f$ is defined by $\mathbf{m}^f = [m_1, m_2, \cdots, m_n]^T$, where m_i is the slip along the ith sub-fault. The data vector $\mathbf{d}^g$ contains the geodetic observables. Each GPS station displacement will add 3 rows to $\mathbf{A}^g$ and 3 elements to $\mathbf{d}^g$, corresponding to the vertical and two horizontal components. In practice, we may choose to ignore the less accurate vertical observation. This is especially true in strike-slip environments where horizontal displacement predominates.

Surface rupture is easily included into (6) by considering measurements of surface displacement as geodetic observation. The offsets are modeled as a priori slip information on the surface intersecting sub-faults. Equation (6) becomes

$$\mathbf{A}\mathbf{m}^f = \begin{bmatrix} \mathbf{A}^g \\ \mathbf{A}^s \end{bmatrix} \mathbf{m}^f = \begin{bmatrix} \mathbf{d}^g \\ \mathbf{d}^s \end{bmatrix} = \mathbf{d} \tag{7}$$

where d_i^s are the discreate approximations of surface slip along the fault trace, and $A_{ij}^s = 1$ if sub-fault element j corresponds to surface slip offset i, otherwise $A_{ij}^s = 0$.

The GPS displacements shown in Figures 4 and 5 are not connected to an external reference but are defined relative to station OCTI. (Some geodetic measurements such as line-length change recorded by EDM observations are independent of an absolute reference.) The displacement at OCTI is assumed to be 0, which in fact may be true from a seismic standpoint since this site is far from the Superstition Hills rupture zone. However, any attempt to use the GPS displacements as a criteria for evaluating the effect of the earthquake sequence will be distorted by measurement error at OCTI and/or non-seismic deformation between this site and the other stations. This ambiguity is largely circumvented if displacement-offset terms are estimated in addition to the fault slip parameters. Equation (7) is then rewritten

$$\mathbf{A}\mathbf{m} = \mathbf{A} \begin{bmatrix} \mathbf{m}^f \\ \mathbf{m}^o \end{bmatrix} = \mathbf{d} \tag{8}$$

where m_i^o is the ith non-seismic component uniformly added to all station displacements (i.e., north, east, vertical).

The Singular Value Decomposition of $\mathbf{A}$ is given by

$$\mathbf{A} = \mathbf{U}\lambda\mathbf{V}^T \tag{9}$$

where $\mathbf{U}$ is a matrix of eigenvectors spanning the data space, $\mathbf{V}$ is a matrix of eigenvectors spanning the parameter space, and λ is a diagonal matrix of singular values. Without loss of generality, this is written

$$\mathbf{A} = \mathbf{U}_p\lambda_p\mathbf{V}_p^T \tag{10}$$

where p refers to the non-zero singular values. If the normal equations of (8) are normalized to have unit variance [e.g., *Segall and Harris*, 1987], the generalized inverse of

(8) and (10) is given by

$$\mathbf{A}^{-1} = \mathbf{V}_p \lambda_p^{-1} \mathbf{U}_p^T \tag{11}$$

[*Lanczos*, 1961; *Menke*, 1984]. In practice it is often necessary to restrict the volume of the parameter space by considering only the k largest singular values, setting all others to 0.

The generalized solution to (8) for the k largest singular values is given by

$$\mathbf{m} = \mathbf{A}_k^{-1}\mathbf{d} + \mathbf{V}_0\alpha_0 \tag{12}$$

where $\mathbf{V}_0$ are eigenvectors spanning the null space of the model and α_0 is a vector of arbitrary coefficients. The volume of the model space not constrained by observation is defined by $\mathbf{V}_0\alpha_0$. This term is not influenced by the geodetic data and is thus arbitrary. Often it is the minimum-length solution $\mathbf{m} = \mathbf{A}_k^{-1}\mathbf{d}$ which is of interest (the coefficients of α_0 are 0). However, some other solution criteria can be satisfied by carefully designating the coefficients of α_0.

For high resolution fault models where the rupture plane is partitioned into numerous sub-faults, it is necessary to apply some type of smoothing constraint over the dislocation surface to prevent the slip distribution from taking on an oscillatory pattern. *Segall and Harris* [1987] showed that the "roughness" of fault slip could be minimized by considering smoothness as an a priori constraint utilized from the model null space through the coefficients of α_0 (Equation 12). They used a smoothing matrix $\mathbf{T}$, with coefficients determined from the discreate approximation of the Laplacian operator $\nabla^2 = \partial^2/\partial x^2 + \partial^2/\partial y^2$, where x and y are the fault distances along strike and dip, respectively. The boundary conditions around the lower and lateral edges of the dislocation are assumed to be null slip, so that the applied smoothing operator causes the calculated fault offset to tend toward zero along these boundarys. Because the Superstition Hills and Elmore Ranch faults ruptured the surface, the upper boundary is

considered an unconstrained dislocation. The estimated fault slip is given by

$$\mathbf{m} = [\mathbf{I} - \mathbf{V}_0(\mathbf{V}_0^T\mathbf{T}^T\mathbf{T}\mathbf{V}_0)^{-1}\mathbf{V}_0^T\mathbf{T}^T\mathbf{T}]\mathbf{A}_k^{-1}\mathbf{d} \qquad (13)$$

(Equation 13, [*Segall and Harris*, 1987]). A similar formulation for utilizing fault smoothness over the model null space is given by *Harris and Segall* [1987]; an alternate method considering fault smoothness as quasi-data is provided by *Snay* [1989].

For over-constrained solutions, where there are more independent data than parameters, if $k = p$ then SVD is equivalent to simple least-squares. This is advantageous since the solution provided by (12) can be utilized for either uniform dislocations or for detailed parameterizations where the fault plane is partitioned into multiple sub-elements.

Simple dislocation theory has the advantage that the displacement and stress/strain fields for simple fault ruptures can be computed almost instantaneously. The inverse problem of using geodetic data to calculate the slip distribution along a fault plane is also straightforward. However, we have assumed the earth can be modeled as a homogeneous half-space. Crustal layering or inhomogeneities in the earth can introduce non-existent structure into half-space models [*Savage*, 1987]. While low-resolution schemes such as the average slip over the fault plane will not be seriously affected, attempts to resolve detailed properties may be badly contaminated by artifacts of earth structure.

Seismic Displacement

We model rupture along the Superstition Hills and Elmore Ranch faults as strike-slip dislocations along vertical planes extending from the surface to 10 km depth. Each dislocation approximately coincides with the mapped surface rupture and/or aftershock distribution. The geometrical parameters for the modeled faults are listed in Table 2.

Initially, the Superstition Hills and Elmore Ranch faults are modeled as uniform dislocations, with no slip variation allowed on the rupture planes. The dislocations are then partitioned into multiple sub-elements and the slip distribution along the two faults is calculated from the discrete offset for each sub-fault.

For an initial estimate of slip along the two faults, we use only the displacements at KANE, MOUN, and L589; the three GPS sites nearest the seismic rupture zone (Figure 7). Because the observed movements at these stations are relative to OCTI, we also solve for uniform north and east-trending offsets in the displacements. This will remove any systematic distortion due to measurement error at OCTI. Both faults are regarded as uniform dislocations. The solution to this simple model is given in Table 3 (Model 1) and the observed vs. calculated displacements are shown in Figure 7. Generally, there is good agreement between model and observation. This is not altogether unexpected since we are solving for 4 parameters with 6 data. The large residual at MOUN is presumably due to the uncertainty in relocating the 1990 reset monument at the 1986 position (recall the estimated error is 15 cm in each direction). The surface deformation pattern computed from Model I is fairly extensive; the 4 cm horizontal displacement contour is shown in Figure 7.

The north and east-trending displacement components at each Imperial Valley site, plotted as a function of distance from a N40°W trending line through OCTI are shown in Figure 8. Shown are the non-seismic movements; that is, the seismic component computed from Model 1 is subtracted from the observed displacements (Figure 4). Stations where the seismic correction is greater than 4 cm (in the component plotted) are shown as open circles, other sites as filled circles. The displacements represent the non-seismic deformation perpendicular to the plate motion.

A fairly well defined pattern is observed in the north-trending components (Figure 8).

Stations to the northeast have moved south (or southeast) about 8.1 cm relative to sites on the other side of the valley. Stations which display the largest deviation are for the most part those sites where the applied seismic correction is greater than 4 cm (open circles). This may indicate fault complexity not accounted for by the simple dislocation used to model the 1987 earthquake. The east-trending displacements, however, show large data scatter; no distinguishable pattern is readily visible across the valley. The scatter is not a function of the magnitude of the applied seismic correction, so presumably it is due to the large measurement errors inherent in the longitudinal direction.

We assume the 8.1 cm north-trending offset is attributed to plate-boundary deformation between the North American and Pacific plates (Figure 8). Taking into account the orientation of the suspected deformation (N40°W), as well as the time interval between the 1986 and 1988 surveys (1.79 years), the north-trending movements suggest 5.9 cm/yr displacement across the valley. This is significantly larger than the 3.45 - 4.3 cm/yr rates obtained from conventional surveys. Although accelerated deformation between the GPS campaigns can not be ruled out, there is relatively poor station coverage in the southwest portion of the valley so it is difficult to precisely estimate the valley crossing displacement. This is especially true considering most of the southwestern sites suffered large seismic displacements during 1987. If Model 1 (Table 3) does not accurately reflect the rupture process during the Superstition Hills earthquake sequence, the unmodeled effects will influence the non-seismic estimate.

The seismic rupture estimated in Model 1 depends heavily on shallow slip since the three stations used are within close proximity to the dislocation planes. While field mapping shows that rupture extended to the surface, slip at depth may go undetected. Therefore, it is necessary to examine the displacement at stations away from the fault to

ascertain the extent of faulting with depth.

To incorporate more GPS data into the fault-plane inversion, it is necessary to remove the non-seismic deformation from the displacement field. Perhaps the best example of secular deformation across the Imperial Valley is provided by U.S.G.S. trilateration measurements between 1972 and 1987 [e.g., *Prescott et al.*, 1987a; *Prescott et al.*, 1987b]. Computed station velocities for the Salton Trough EDM network are roughly parallel to the direction of plate motion (N40°W) (Figure 9), although to some degree the geodetic orientation is dictated by the outer coordinate solution imposed to transform EDM line-length changes into station displacements [*Prescott*, 1981]. The total differential velocity across the network is 3.45 cm/yr and is accommodated in a 50 km wide zone [*Prescott et al.*, 1987b]. Triangulation measurements suggest a larger rate between 1941 and 1986 (4.3 cm/yr), but these observations are not as accurate as the EDM measurements [*Snay and Drew*, 1988]. However, along the Imperial fault where EDM sites are sparse, the triangulation data suggest concentrated deformation in a narrow 20 km wide zone. The conventional geodetic data are modeled using the following empirical approach. The differential velocity across the valley is assumed to be 3.45 cm/yr. Running along the axis of the valley is a transition zone(s) (Figure 9), where the strain gradient is defined by simple shear with the displacements oriented N40°W. The transition zone north of the Imperial fault is 50 km wide; to the south it is 20 km wide. The modeled station movements fit the observed EDM displacements extremely well (Figure 9).

The secular deformation derived from the conventional measurements is subtracted from the observed GPS displacements (Figures 4 and 5), leaving the seismic component (and measurement error). For Model 2 (Table 3), the uniform slip along the Superstition Hills and Elmore Ranch faults is recomputed using all GPS data (without the secular

deformation). The residuals (observed minus calculated) for this model are shown in Figure 10. The largest residuals trend in the longitudinal direction and are especially noticeable for those sites in the southeast. This reconfirms our speculation for large east-trending errors. However, the residual vectors at the three stations nearest the seismogenic zone are unusually large. The large vector at MOUN is easily explained since this station was reset between surveys. The residuals at L589 and KANE, however, are significantly larger than the average residual computed at the other stations. Field inspection at both localities revealed no evidence that either monument had been disturbed. Because both sites are located near the seismic rupture zone, this suggests additional slip not accounted for by the simple dislocation parameters used for Model 2.

Although the estimated slip is marginally different between Models 1 and 2 (Table 3), this is not significant considering the estimated uncertainties. In fact, because the near-field (Model 1) and far-field (Model 2) solutions are similar, this suggests that to first order there is not significant slip dependence with depth (within a factor of 2 or 3). It is also noteworthy that the uncertainties improve by only ~ 50 % with the additional data supplied with Model 2. This illustrates the necessity of measurements near the seismic rupture. For simple fault models, where uniform slip is constrained to a single dislocation plane (or two planes in the case of the Superstition Hills sequence), it is as important to have at least minimal station coverage within a few kilometers of the seismogenic zone, as it is to have many sites located away from the fault(s).

Seismic Slip Distribution

Uniform dislocations for the Superstition Hills and Elmore Ranch faults were utilized for Models 1 and 2. To estimate the seismic slip distribution, it is necessary to partition the rupture planes into multiple regions or sub-faults (Model 3). The divisions must be sufficiently dense as to provide reasonable slip resolution. We choose 10 sub-fault

elements in the horizontal and 5 in the vertical, so that each fault is partitioned into 50 sub-regions. The dimensions of each dislocation element is 2.0 km in width (vertical) and about 2.5 km in length (2.4 km for Superstition Hills and 2.6 km for the Elmore Ranch fault). The slip distribution along the two rupture planes is constrained to be sufficiently smooth (Equation 13). The GPS displacements are adjusted according to the estimated north and east-trending offsets estimated for Model 2.

In addition to the GPS data, a priori surface-slip information is added to the solution. Surface slip along the Superstition Hills fault extends (nearly) the entire length of the modeled fault plane (Figure 11) [*Williams and Magistrale*, 1989]. The surface rupture has been incremented into 2.4 km segments corresponding to the horizontal dimension of each sub-fault. The average slip over each segment is assigned as an a priori slip estimate for the surface fault element to which it corresponds. Surface rupture along the Elmore Ranch fault is confined to the southwestern segment (Figure 11). Recall for this event that the mapped surface breaks occurred along several nearly parallel strands (Figure 2) [*Hudnut et al.*, 1989a]. We take the cumulative surface offset for all strands averaged over 2.6 km segments, and use this as a priori slip for the surface sub-fault elements. Where no rupture is mapped (to the northeast), the surface intersecting fault partitions are assigned 0 slip. The a priori uncertainty for each surface-slip estimate is assumed to be 10 cm.

The number of independent parameters estimated through singular value decomposition depends on the number of singular values k utilized in Equation (12). A trade-off exists between solution variance and resolution [e.g., *Menke*, 1984]. While large k produces highly resolved models, this is at the expense of increasing solution uncertainty. Correspondingly, small k yields low variance solutions but does not provide detailed resolution. A total of 100 sub-fault elements are use for Model 3 (50 for each

fault). If $k = 100$, then slip along each sub-fault will be determined uniquely. Because of limited geodetic coverage, however, it is practical to consider only the first few eigenvectors of the parameter space defined by the geodetic observations. Therefore, each solved parameter is a function of some combined slip over multiple sub-fault elements. This is a fundamental property of singular value decomposition when used to solve under-determined or poorly-determined problems [e.g., *Jackson*, 1972]. It is necessary to determine the k which maximizes the resolution without allowing the solution to become too oscillatory or unstable.

The geodetic moment, solution instability, and model residual calculated for different values of k are shown in Figure 12. The moment is a function of the average slip along the fault planes, while solution instability is determined from the standard deviation of slip for each sub-fault element. An instability of 0 (stable) indicates uniform slip along the fault planes, while high values indicate an oscillatory or unstable solution. The RMS indicates the agreement between model and observation and is calculated by $\mathrm{RMS} = \sum(o_i - c_i)^2/\sigma_i^2$ where o_i is the observed, c_i is the calculated, and σ_i is the uncertainty assigned to the ith observation.

When surface slip is incorporated into the solution (Figure 12a), the first 20 singular values are well constrained by the measured offset along the fault, and are influenced little by the geodetic observations. The surface measurements reflect the dislocation on the uppermost fault elements, with little depth resolution. This is illustrated by the solution for $k = 20$. The calculated moments are significantly less than that for Model 2, presumably because the surface offset is not representative of the larger displacement along the rest of the fault plane(s). Consequently, in order to estimate the slip distribution with depth it is necessary to consider solutions where $k > 20$. The solution becomes increasingly oscillatory after $k = 30$ as is indicated by the instability. The RMS

is significantly reduced beyond k = 20, but only improves marginally with increasing *k*. The solution fit for k > 20 is slightly better than that for Model 2.

Also evident in Figure 12a are the large moment estimates for the Elmore Ranch fault, which are almost equal to the computed moments for the Superstition Hills fault. This is unexpected considering the latter event yielded a significantly greater surface wave magnitude, as well as a larger moment estimated from Model 2. It is difficult to distinguish slip between the two faults using SVD, as is illustrated by Figure 13. The displacement pattern for a 130 cm rupture on the northwest-trending right-lateral Superstition Hills fault is compared with a 30 cm rupture on the northeast-trending left-lateral Elmore Ranch fault. The deformation pattern between the two dislocations is almost identical (although different in magnitude). As a result, the larger slip estimate along the Superstition Hills fault is being mapped onto the Elmore Ranch fault plane producing the higher moment. This is especially true since only the first few model-space eigenvectors are used, as is necessary because Model 3 is very underdetermined (more model parameters than data). Therefore, only linear combinations of model parameters are uniquely defined. The similar moments indicated by Figure 12a suggest slip between the two faults is strongly correlated.

The estimated seismic slip distribution along the Superstition Hills and Elmore Ranch faults for k = 23 and k = 27 are shown in Figure 14a. We refer to these solutions as Models 3a and 3b, respectively (Table 3). Although both faults are partitioned into 50 elements, the fault-rupture is not as resolved as the contours suggest since only the first few (non-surface) model-space eigenvectors are independently solved. The solution suggests fairly uniform rupture along both fault planes for k = 23. The dislocation may be slightly concentrated to the southwest along the Elmore Ranch fault. The apparent "bullseye" pattern is due to the smoothness constraint, which requires zero slip along the

lateral edges and lower boundaries (the upper boundaries are constrained by the surface slip). There is little difference in the slip distribution for $k=21$ through $k=26$. However, there is a noticeable change in the dislocation pattern starting with $k=27$. While slip along the Elmore Ranch fault still appears fairly uniform, displacement along the Superstition Hills fault is concentrated to the northwest and to the southeast. This change is significant and is caused by the GPS displacement at one station. Recall the large residual for L589 in Model 2 (Figure 10). This discrepancy is nearly eliminated beginning with $k=27$. Therefore, in order to satisfy the observed displacement at L589, it is necessary to concentrate rupture at each end of the Superstition Hills fault. This analysis assumes the observed GPS displacement at L589 is seismically generated, and not contaminated by an unusually large measurement error. The slip deficit near the center of the fault roughly corresponds to the drop in slip measured at the surface (Figure 11).

Independent solutions are made without constraining the upper sub-fault elements by surface offset measurements (Figure 12b). The unconstrained moments are generally smaller than when surface slip is used. This is because the surface measurements are less than the average slip estimate along the fault plane. Without surface constraint, the geodetic data are satisfied to a greater degree by slip near the surface; otherwise, it is necessary to compensate the small shallow offsets by increased slip at greater depths. The seismic slip distribution estimated without surface constraint along the Superstition Hills and Elmore Ranch faults for $k=3$ and $k=7$ are shown in Figure 14b. We refer to these solutions as Models 3c and 3d, respectively (Table 3). For these unconstrained solutions, the slip distribution is confined to shallower depths. Nevertheless, the solution for $k=7$ yields concentrated slip at each end of the Superstition Hills fault. This emphasizes that the calculated slip discrepancy near the faults midsection is not simply an artifact of incorporating measurements of surface offset into the model.

6. Geophysical Implications

Conjugate Faulting

The most prominent feature of the Superstition Hills earthquake sequence is the conjugate relationship exhibited by near-simultaneous ruptures along right-lateral northwest and left-lateral northeast-trending faults. In the context of the Imperial Valley, the northeast-trending structures are termed "cross-faults" [e.g., *Hudnut et al.*, 1989a]. Conjugate and cross-fault seismicity seems to be a fairly typical phenomenon for this region (Figure 15), and may dictate the strain transfer mechanism between faults. The 1981 Westmorland earthquake (M_L 4.1) is a prime example of cross-fault tectonics. The mainshock and aftershock sequence is clearly mapped onto a northeast-trending lineament. Other examples are associated with the Imperial fault. The largest aftershock (M_L 5.8) following the 1979 Imperial Valley earthquake (M_L 6.6) was located near the town of Brawley [*Johnson and Hutton*, 1982]. The focal mechanism and following seismicity suggested left-lateral slip along a vertical northeast-trending fault. *Reilinger and Larsen* [1986] found that rupture along an identical conjugate structure successfully modeled geodetic observations within the Brawley Seismic Zone. A large (M_L 5.5) aftershock was also recorded near Brawley following the 1940 earthquake [*Neumann*, 1942]. Due to the sparsity of seismic data, neither the mechanism nor location are precisely determined, although we speculate this event occurred along the same northeast-trending feature as the large 1979 aftershock. Of historical interest are Imperial Valley earthquake pairs during 1915 (M_L 6.3, M_L 6.3) and 1927 (M_L 5.8, M_L 5.5) [*Beal*, 1915; *Toppozada et al.*, 1978]. In each case, the 2nd shock followed the first by about 1 hour, contrasting with the 12 hour interval between the 1987 events. It is not known which fault(s) ruptured during these earthquake sequences, but conjugate fault interaction is highly probable.

Rupture on the Superstition Hills fault was almost certainly triggered by the Elmore Ranch event (occurring 12 hours earlier) suggesting some mechanism of stress transfer between the two faults. Figure 16 shows the normal (σ_n) and strike-shear (σ_S) stress components instantaneously applied to the Superstition Hills fault due to a 30 cm left-lateral Elmore Ranch dislocation (Model 2). Tension and right-lateral shear are considered positive, both tending to induce failure on the rupture plane. Also shown is the Coulomb failure stress (σ_c), here given by $\sigma_c = \sigma_s + \mu\sigma_n$, where $\mu = 0.75$. Positive values indicate stress-loading leading toward shear failure.

The stress regime necessary for left-lateral rupture along a northeast-trending fault is identical to that required for right-lateral failure along a northwest-trending fault. Hence, we can assume that the Superstition Hills rupture plane was at or near failure at the time of the Elmore Ranch event. The initial shock generated an increase in the Coulomb failure potential along the Superstition Hills fault (Figure 16), possibly advancing it past its failure threshold. This is seen mostly as a combination of reduced compressive stress (earthquake inducing) countered by left-lateral shear (earthquake inhibiting). The increase is maximized along the northwest boundary of the rupture plane, near the nucleation point of the second event. Presumably rupture began where the applied stress was greatest and then propagated to the southeast. Northwestward rupture is prohibited because the increase in compressive forces tends to inhibit shear failure along this segment of the plane. The magnitude of the Coulomb stress increase near the Superstition Hills epicentral zone ($\sim$ 10 bars) is comparable to typical earthquake stress drops.

The one to several hour delay recorded between events during observed and suspected conjugate episodes in the Imperial Valley is significant from an earthquake failure perspective. Shown in Figure 17 are potential scenario's for earthquake ruptures

involving conjugate-mainshock interaction, such as that observed for the Superstition Hills events. We assume faults fail by an undefined mechanism when they are at or above some critical stress level. The regional strain acting over several years brings a fault near this critical failure point. A stress increase is induced along part of the fault plane due to rupture on a conjugate structure (e.g., Figure 16), which may or may not be sufficient to push the stress state past its critical threshold. In the case of Earthquake 1 (Figure 17a), the stress change caused by the conjugate event is not enough to induce failure. Some form of time dependent stress transfer onto the fault is activated and eventually the critical level is reached. Such a mechanism involving postseismic viscous creep along the Elmore Ranch fault has been suggested for the 1987 Superstition Hills sequence [*Given and Stuart*, 1988]. If this scenario is valid, we would equally expect failure modes such as that indicated by Earthquake 2. Here, the instantaneous stress applied to the fault from the conjugate event pushes the stress state past the critical level and rupture is immediate. In this case, failure along the two perpendicular fault planes will occur simultaneously. However, this behavior is not observed in the Imperial Valley. Conjugate episodes characteristically have been separated by one to several hours. This suggests that the critical stress level can be exceeded without immediate failure. Therefore, some time dependent mechanism must be active on the fault plane, as opposed to additional stress transfer through the crust. We loosely refer to this as "stress corrosion" (Figure 17b) [e.g., *Das and Scholz*, 1981]. In the case of Earthquakes 3 and 4, it is suggested that the critical stress level must be exceeded for a period of one to several hours before failure occurs. *Hudnut et al.* [1989b] proposed fluid diffusion as an alternate mechanism, whereby the effective normal stress was reduced (made more positive) due to pore-fluid infiltration into the rupture plane, thus increasing the Coulomb failure stress. This process still involves action on the fault plane rather than stress transfer. Regardless of cause, the temporal and geometric relationship exhibited

by the conjugate fault interaction is seemingly typical of Imperial Valley tectonics, and is thus an important factor for the potential prediction of large earthquakes and aftershocks.

Moment and slip distribution

The geodetic (GPS) source parameters for the Superstition Hills and Elmore Ranch earthquakes are listed in Table 3 and Figure 14. The seismic moment is best defined by Model 2, while the slip distribution is best expressed by Models 3a and 3b. Model 1 is constrained with minimal station coverage and Models 3c and 3d do not include the additional information supplied from surface slip measurements. The GPS observations are directly proportional to the combined effect of the Elmore Ranch and Superstition Hills events, although we have attempted to resolve slip between each fault. The calculated parameters are a function of the coseismic offset, as well as 3 - 4 months of postseismic slip (plus 1.5 years of preseismic movement, if any). The average left-lateral Elmore Ranch dislocation is about 30 cm, with fairly uniform distribution along the fault plane. In the case of the Superstition Hills fault, the average right-lateral slip is about 130 cm, with concentrated deformation along the northwest and southeast sections of the fault. Because the GPS sampling frequency is so low (years), the calculated source parameters should contain the total coseismic moment, including several months of postseismic slip.

The GPS moments are compared with estimates made through seismic and other geodetic studies (Table 4). Forward and inverse models using teleseismic and strong-motion recordings are used to constrain source parameters, as well as investigate complexities of the Superstition Hills rupture process [*Dziewonski et al.*, 1989; *Bent et al.*, 1989; *Sipkin*, 1989; *Frankel and Wennerberg*, 1989; *Wald et al.*, 1990; *Hwang et al.*, 1990]. The teleseismic moments agree fairly well with the GPS estimates, while the strong

ground motion data suggest significantly lower moments. The high-frequency strong-motion measurements are dominated by energy around 1 second and conceivably miss a sizable portion of the long-period energy release recorded with the teleseismic and GPS data. Hence, the near field seismic solutions may underestimate the total moment release.

Geodetic measurements from Pinyon Flat observatory are used to constrain planer and curved dislocation models for the Superstition Hills and Elmore Ranch faults [*Agnew and Wyatt*, 1989]. The data are obtained from long-base strain and tilt-meters, as well as a borehole dilatometer. The best-fit planer models to all observations are significantly lower than those calculated with the GPS and teleseismic data (Table 4), although a 70 % moment increase for the Superstition Hills fault is obtained when the strainmeter data are excluded. The low moment estimate may be due to a number of factors [*Agnew and Wyatt*, 1989]: 1) measurement quality, particular with the strainmeter, 2) rheologic differences between Superstition Hills and Pinyon Flat, and 3) strainmeter-dilatometer sensitivity to the nodal deformation plane roughly on azimuth with the observatory.

Geodolite observations from the Salton Trough EDM network were made in early December (1987), several days after the two large earthquakes [*Lisowski and Savage*, 1988]; the last previous occupation was in January, 1987. Simple dislocation models with 40 cm left-lateral slip along the Elmore Ranch fault and 120 cm right-lateral slip along the Superstition Hills fault best-fit the observations. The estimated moment for the Superstition Hills event is comparable to that obtained with the GPS displacements (Table 4).

The discrepancies in Table 4 are largely attributed to the alternate methodologies, observations, and parameters used to constrain each model. However, for those calculations which include moment estimates for both the Superstition Hills and Elmore

Ranch events, the ratio between the two ruptures is fairly constant. This illustrates an internal consistency with each method. More importantly, it suggests that postseismic slip along the Superstition Hills fault is probably confined to the shallow segment of the rupture plane. Since seismic activity on the Elmore Ranch fault essentially ceased after the 2nd main event, if postseismic slip were occurring in mass along a large fraction of the Superstition Hills rupture plane, the GPS moment ratio would be considerably larger.

While the epicenter and aftershock sequence for the Superstition Hills event were concentrated along the northwestern portion of the fault, seismic and surface slip data suggest significant moment release on the southern section of the Superstition Hills fault [*Wald et al.*, 1989; *Bent et al.*, 1989; *Hwang et al.*, 1990; *Williams and Magistrale*, 1989]. An exception is the strong ground motion study of *Frankel and Wennerberg* [1989], where slip is confined to the northwest. However, their low Superstition Hills moment (Table 4) suggests this analysis may be strongly susceptible to the high-frequency content of the data, indicating rupture along the southeast segment was dictated primarily by low-frequency energy release. The GPS data also reveal dislocation along the southeastern segment of the fault, and further suggests a displacement null near the faults mid-section. This slip deficiency may be related to the surface offset drop observed along the center of the fault (Figure 10).

Deformation across the Imperial Valley

The 1986-1988 GPS station displacements indicate a significant component of deformation across the Imperial Valley not associated with the 1987 Superstition Hills earthquake sequence (Figures 4 and 8). This motion is attributed to plate-boundary deformation due to the relative velocity between the Pacific and North American plates. From empirical evidence provided by Salton Trough EDM observations between 1972 and 1987, these non-seismic movements were modeled as 3.45 cm/yr differential velocity

across the valley. However, after removing the seismic deformation predicted with a preliminary model (Model 1, Table 4) the calculated GPS displacements average 5.9 cm/yr (Figure 8), significantly larger than that obtained with the trilateration measurements over the last two decades. This GPS velocity is also larger than the 4.7 cm/yr plate motion predicted from global models (for Imperial Valley coordinates) [*DeMets et al.*, 1990]. The GPS rate may be an overestimate, especially considering the large measurement uncertainties and the influence from the 1987 earthquake sequence. It is possible, however, that the 1986-1988 GPS rate could represent accelerated deformation. In fact, GPS observations between 1988 and 1989 indicate 5.2 $\pm$ 0.9 cm/yr displacement across the Imperial Valley [*Larsen and Reilinger*, 1991]. Accelerated deformation is not without precedence. Triangulation observations suggest a rate of 6.2 cm/yr between 1941 and 1954, although this is attributed to postseismic deformation following the 1940 Imperial Valley earthquake. Increased deformation following the 1979 earthquake is not observed in the EDM observations [*Savage et al.*, 1986]. Additional GPS measurements are necessary in the Imperial Valley in order to ascertain the current deformation rate.

7. Conclusions

Station movements computed from 4 Imperial Valley GPS campaigns indicate large crustal displacements during the periods 1986-1988 and 1986-1990. Much of the deformation is attributed to the 1987 Superstition Hills earthquake sequence. Ten sites near the seismic rupture zone are displaced at least 10 cm, although the GPS observations contain large uncertainties. This is the first occurrence of a large earthquake within a preexisting GPS network.

The 1987 earthquake sequence is initially modeled as uniform offsets along

rectangular dislocations in an elastic half-space. The best-fit model to the GPS observations requires 130 cm right-lateral slip along the northwest-trending Superstition Hills fault and 30 cm left-lateral motion along the conjugate northeast-trending Elmore Ranch fault. The slip distribution along each fault is investigated by partitioning the rupture planes into 50 sub-elements and utilizing Singular Value Decomposition to estimate the slip along each sub-fault. Measurements of surface offset are used to constrain slip on the shallow elements of the fault plane. The estimated slip distribution along the Elmore Ranch fault is fairly uniform. Slip along the Superstition Hills fault appears to be concentrated to the northwest and the southeast, with a displacement drop near the faults midsection. The estimated geodetic moments are 9.4×10^{25} dyne-cm and 2.3×10^{25} dyne-cm for the Superstition Hills and Elmore Ranch faults, respectively. These moments are consistent with those obtained from teleseismic data, suggesting that postseismic slip along the Superstition Hills fault was concentrated near the surface.

In addition, the 1986-1988 GPS observations suggest non-seismic movements across the Imperial Valley of up to 5.9 cm/yr. These secular displacements are attributed to plate-boundary deformation due to the relative motion between the North American and Pacific plates. The observed rate is probably an overestimate, however, as it is heavily influenced by unmodeled seismic effects and measurement error. Regardless, the observed seismic and secular deformations clearly emphasize the importance of future GPS study in the Imperial Valley.

Acknowledgements

The field support provided by so many people has proven invaluable. In particular we thank John Beavan, Lewis Gilbert, Ken Hudnut, Michael Jackson, and Mike Bevis. We also thank William Young and Gerald Dole at the Riverside County Flood Control District and Gerald Stayner at the Riverside County Survey Department for providing support for the 1990 mini-campaign. Ken Hudnut processed the 1990 data. Reviews by Hiroo Kanamori, Kerry Sieh, and William Prescott substantially improved the manuscript. This work is supported by U.S.G.S. grants 14-08-0001-61679 (MIT) and 14-08-001-61354 (Caltech), and by NASA contracts NAG-5-814 (MIT) and NAG-5-842 (Caltech). Caltech Division of Geological and Planetary Sciences contribution number 4980.

References

Agnew, D. C., and F. K. Wyatt, The 1987 Superstition Hills earthquake sequence: Strains and tilts at Pinon Flat observatory, *Bull. Seismol. Soc. Am.*, *79*, 480-492, 1989.

Alewine, R. W., Application of linear inversion theory toward the estimation of seismic source parameters, Ph.D. Thesis, California Institute of Technology, Pasadena, 303 pp., 1974.

Beal, C. H., The earthquake in the Imperial Valley, California, June 22, 1915, *Bull. Seismol. Soc. Am.*, *5*, 130-149, 1915.

Bent, A. L., D. V. Helmberger, R. J. Stead, and P. Ho-Liu, Waveform modeling of the November 1987 Superstition Hills earthquakes, *Bull. Seismol. Soc. Am.*, *79*, 500-514, 1989.

Beutler, G., W. Gurtner, I. Bauersima, and R. Langley, Modeling and estimating the orbits of GPS satellites, paper presented at First International Symposium on Precise Positioning with the Global Positioning System, Int. Assoc. of Geod., Rockville, Md., April 15-19, 1985.

Budding, K. E., and R. V. Sharp, Surface faulting associated with the Elmore Ranch and Superstition Hills, California, earthquake of 24 November 1987, *Seismol. Res. Letts.*, *59*, p. 49, 1988.

Chinnery, M. A., The deformation of the ground around surface faults, *Bull. Seismol. Soc. Am.*, *51*, 355-372, 1961.

Chinnery, M. A., The stress changes that accompany strike-slip faulting, *Bull. Seismol.*

Soc. Am., *53*, 921-932, 1963.

Das, S., and C. H. Scholz, Off-fault aftershock clusters caused by shear stress increase?, *Bull. Seismol. Soc. Am.*, *71*, 1669-1675, 1981.

Davis, J. L., W. H. Prescott, J. L. Svarc, and K. J. Wendt, Assessment of global positioning system measurements for studies of crustal deformation, *J. Geophys. Res.*, *94*, 13,635-13,650, 1989.

Defense Mapping Agency, Department of Defense world geodetic system 1984, *DMA TR 8350.2*, D.M.A. Washington, D. C., 122 pp., 1987.

DeMets, C., R. G. Gordon, S. Stein, and D. F. Argus, A revised estimate of Pacific-North America motion and implications for western North America plate boundary zone tectonics, *Geophys. Res. Letts.*, *14*, 911-914, 1987.

DeMets, C., R. G. Gordon, D. F. Argus, and S. Stein, Current plate motions, *Geophys. J. Inter.*, *101*, 425-478, 1990.

Dong, D., and Y. Bock, Global positioning system network analysis with phase ambiguity resolution applied to crustal deformation studies in California, *J. Geophys. Res.*, *94*, 3949-3966, 1989.

Drew, A. R., and R. A. Snay, DYNAP: software for estimating crustal deformation from geodetic data, *Tectonophysics*, *162*, 331-343, 1989.

Dziewonski, A. M., G. Ekstrom, J. H. Woodhouse, and G. Zwart, Centroid-moment tensor solutions for October-December 1987, *Phys. Earth Planet. Inter.*, *54*, 10-21, 1989.

Elders, W. A., R. W. Rex, T. Meidav, P. T. Robinson, and S. Biehler, Crustal spreading

in southern California, *Science, 178*, 15-24, 1972.

Frankel, A., and L. Wennerberg, Rupture process of the M_S 6.6 Superstition Hills earthquake determined from strong-motion recordings: Application of tomographic source inversion, *Bull. Seismol. Soc. Am., 79*, 515-541, 1989.

Fuis, G. S., W. D. Mooney, J. H. Healey, G. A. McMechan, and W. J. Lutter, Crustal structure of the Imperial Valley region, *U.S. Geol. Surv. Prof. Pap., 1254*, 25-50, 1982.

Given, D. D., and W. D. Stuart, A fault interaction model for triggering of the Superstition Hills earthquake of November 24, 1987, *Seismol. Res. Letts., 59*, p. 48, 1988.

Gurtner, W., G. Beutler, I. Bauersima, and T. Schildknecht, Evaluation of GPS carrier difference observations: The Bernese second generation software package, paper presented at First International Symposium on Precise Positioning With the Global Positioning System, Int. Assoc. of Geod., Rockville, Md., April 15-19, 1985.

Harris, R. A., and P. Segall, Detection of a locked zone at depth on the Parkfield segment of the San Andreas fault, *J. Geophys. Res., 92*, 7945-7962, 1987.

Hudnut, K. W., L. Seeber, T. Rockwell, J. Goddmacher, R. Klinger, S. Lindvall, and R. McElwain, Surface ruptures on cross-faults in the 24 November 1987 Superstition Hills, California, earthquake sequence, *Bull. Seismol. Soc. Am., 79*, 282-296, 1989a.

Hudnut, K. W., L. Seeber, and J. Pacheco, Cross-fault triggering in the November 1987 Superstition Hills earthquake sequence, southern California, *Geophys. Res. Letts., 16*, 199-202, 1989b.

Hudnut, K., and M. Clark, New slip along parts of the 1968 Coyote Creek fault rupture, California, *Bull. Seismol. Soc. Am.*, *79*, 451-465, 1989.

Hwang, L. J., H. Magistrale, and H. Kanamori, Teleseismic source parameters and rupture characteristics of the 24 November 1987, Superstition Hills earthquake, *Bull. Seismol. Soc. Am.*, *80*, 43-56, 1990.

Ingle, J. C., Paleobathymetric history of Neogene marine sediments, northern Gulf of California, *in* Geology of Peninsular California, Pacific Sections AAPG, SEPM, and SEG, 121-138, 1974.

Iwasaki, T., and R. Sato, Strain field in a semi-infinite medium due to an inclined rectangular fault, *J. Phys. Earth*, *27*, 285-314, 1979.

Jackson, D. D., Interpretation of inaccurate, insufficient and inconsistent data, *Geophys. J. R. Astron. Soc.*, *28*, 97-107, 1972.

Johnson, C. E., and D. P. Hill, Seismicity of the Imperial Valley, *U.S. Geol. Surv. Prof. Pap.*, *1254*, 14-24, 1982.

Johnson, C. E., and L. K. Hutton, Tectonic implications of the November 24, 1987, Superstition Hills earthquakes, Imperial Valley, CA, *Seismol. Res. Letts.*, *59*, p. 48, 1988.

King, R. W., E. G. Masters, C. Rizos, A. Stolz, and J. Collins, *Surveying with GPS, Monograph 9*, School of Surveying, The University of New South Wales, Kensington, Australia, 128 pp., 1985.

Lanczos, C., *Linear Differential Operators*, D. Van Nostrand, New York, 1961.

Larsen, S. C., Geodetic measurement of deformation in southern California, California

Institute of Technology, Ph.D. thesis, 351 pp., 1991.

Larsen, S. C., R. E. Reilinger, GPS measurements of strain accumulation across the Imperial Valley, California: 1986-1989, in preparation, 1991.

Larsen, S. C., D. C. Agnew, B. H. Hager, Strain accumulation in the Santa Barbara channel: 1971-1987, in preparation, 1991.

Larson, P. A., H. W. Menard, and S. M. Smith, Gulf of California: A result of ocean-floor spreading and transform faulting, *Science, 161*, 781-784, 1968.

Lichten, S. M., and J. S. Border, Strategies for high-precision Global Positioning Systems orbit determination, *J. Geophys. Res., 92*, 12,751-12,762, 1987.

Lisowski, M., and J. C. Savage, Deformation associated with the Superstition Hills, California, earthquakes of November 1987, *Seismol. Res. Letts., 59*, p. 35, 1988.

Lomnitz, C., F. Mooser, C. R. Allen, J. N. Brune, and W. Thatcher, Seismicity and tectonics of northern Gulf of California region, Mexico: Preliminary results, *Geofis. Int., 10*, 34-48, 1970.

Magistrale, H., L. Jones, and H. Kanamori, The Superstition Hills, California, earthquakes of 24 November, 1987, *Bull. Seismol. Soc. Am., 79*, 239-251, 1989.

Mansinha, L., and D. E. Smylie, Effect of earthquakes on the Chandler wobble and the secular polar shift, *J. Geophys. Res., 72*, 4731-4743, 1967.

Mansinha, L., and D. E. Smylie, The displacement fields of inclined faults, *Bull. Seismol. Soc. Am., 61*, 1433-1440, 1971.

McGill, S. F., C. R. Allen, K. W. Hudnut, D. C. Johnson, W. F. Miller, and K. E. Sieh,

Slip on the Superstition Hills fault and on nearby faults associated with the 24 November 1987 Elmore Desert Ranch and Superstition Hills earthquakes, southern California, *Bull. Seismol. Soc. Am.*, *79*, 362-375, 1989.

Menke, W., *Geophysical Data Analysis: Discrete Inverse Theory*, Academic, Orlando, Fla., 1984.

Moore, D. G., and E. C. Buffington, Transform faulting and growth of the Gulf of California since late Pliocene, *Science*, *161*, 1238-1241, 1968.

Neumann, F., United States earthquakes, 1940, *U.S. Coast and Geod. Sur. Serial*, *647*, 74 pp., 1942.

Okada, Y., Surface deformation due to shear and tensile faults in a half-space, *Bull. Seismol. Soc. Am.*, *75*, 1135-1134, 1985.

Prescott, W. H., The determination of displacement fields from geodetic data along a strike slip fault, *J. Geophys. Res.*, *86*, 6067-6072, 1981.

Prescott, W. H., J. C. Savage, and M. Lisowski, Crustal strain, in National Earthquake Hazards Reduction Program, Summaries of Technical Reports, *U.S. Geological Survey Open-File Report*, *87-374*, 272-280, 1987a.

Prescott, W. H., M. Lisowski, and J. C. Savage, Velocity field along the San Andreas fault in southern California, *EOS Trans.*, *68*, p. 1506, 1987b.

Reilinger, R. E., and S. C. Larsen, Vertical crustal deformation associated with the 1979 M = 6.6 Imperial Valley, California earthquake: Implications for fault behavior, *J. Geophys. Res.*, *91*, 14,044-14,056, 1986.

Rocken, C., The global positioning system: A new tool for tectonic studies, Ph.D. Thesis,

University of Colorado, Boulder, 365 pp., 1988.

Savage, J. C., and L. M. Hastie, Surface deformation associated with dip-slip faulting, *J. Geophys. Res.*, *71*, 4897-4904, 1966.

Savage, J. C., W. H. Prescott, and G. Gu, Strain accumulation in southern California, 1973-1984, *J. Geophys. Res.*, *91*, 7455-7473, 1986.

Savage, J. C., Effect of crustal layering upon dislocation modeling, *J. Geophys. Res.*, *92*, 10,595-10,600, 1987.

Segall, P., and R. Harris, Earthquake deformation cycle on the San Andreas fault near Parkfield, California, *J. Geophys. Res.*, *92*, 10,511-10,525, 1987.

Sipkin, S. A., Moment-tensor solutions for the 24 November 1987 Superstition Hills, California earthquake, *Bull. Seismol. Soc. Am.*, *79*, 493-499, 1989.

Snay, R. A., Enhancing the geodetic resolution of fault slip by introducing prior information, *Manuscripta Geodaetica*, *14*, 391-403, 1989.

Snay, R. A., and A. R. Drew, Supplementing geodetic data with prior information for crustal deformation in the Imperial Valley, California, Technical Report Series, University of Stuttgart, 30 pp., 1988.

Steketee, J. A., On Volterra's dislocations in a semi-infinite medium, *Can. Jour. Phys.*, *36*, 192-205, 1958.

Toppozada, T. R., D. L. Parke, and C. T. Higgins, Seismicity of California 1900-1931, *Calif. Div. of Mines and Geol Spec. Rep.*, *135*, 39 pp., 1978.

U.S. Geological Survey, The Imperial Valley, California, earthquake of October 15, 1979,

U.S. Geol. Surv. Prof. Pap., 1254, 451 pp., 1982.

Wald, D. J., D. V. Helmberger, S. H. Hartzell, Rupture process of the 1987 Superstition Hills earthquake from the inversion of strong motion data, *Bull. Seismol. Soc. Am.*, in press, 1990.

Ward, S. N., and S. E. Barrientos, An inversion for slip distribution and fault shape from geodetic data observations of the 1983, Borah Peak, Idaho, earthquake, *J. Geophys. Res.*, *91*, 4909-4919, 1986.

Wells, D., N. Beck, D. Delikaraoglou, A. Kleusberg, E. J. Krakiwsky, G. Lachapelle, R. B. Langley, M. Nakiboglu, K. Schwarz, J. M. Tranquilla, and P. Vanicek, *Guide to GPS Positioning*, Canadian GPS Associates, Fredericton, N. B., Canada, 1987.

Williams, P. L., and H. W. Magistrale, Slip along the Superstition Hills fault associated with the 24 November 1987 Superstition Hills, California, earthquake, *Bull. Seismol. Soc. Am.*, *79*, 390-410, 1989.

Table 1. Imperial Valley GPS Campaign Summary

Year	Month	Days	Stations	Organization
1986	May/June	20	42	NGS
1988	February/March	9	19	UNAVCO
1988	March/April	6	21	NGS
1990	April	1	3	UNAVCO/RCFC

NGS - National Geodetic Survey
UNAVCO - University Navstar Consortium
RCFC - Riverside County Flood Control

Table 2. Parameters for Modeled Dislocations

	Superstition Hills	Elmore Ranch
Length (km)	25	25
Width (km)	10	10
Strike	N50°W	N40°E
Dip	90	90
Depth (km)	0	0
Latitude (°N)	32.9569	33.1078
Longitude (°E)	-115.7431	-115.7505

Latitude and Longitude are coordinates
at top center of dislocation
Depth is depth to top of fault

Table 3. Inverse Models of Seismic Slip

Model	Fault	Sub-faults		Slip	Moment
		Strike	Dip	(cm)	($x10^{25}$ dyne-cm)
Model 1	SH	1	1	109. ± 13.	7.8
Model 1	ER	1	1	-45. ± 19.	3.4
Model 2	SH	1	1	130. ± 8.	9.4
Model 2	ER	1	1	-30. ± 10.	2.3
Model 3a	SH	10	5		9.9
Model 3a	ER	10	5		5.9
Model 3b	SH	10	5		8.4
Model 3b	ER	10	5		7.0
Model 3c	SH	10	5		6.2
Model 3c	ER	10	5		3.9
Model 3d	SH	10	5		9.2
Model 3d	ER	10	5		4.9

SH - Superstition Hills fault
ER - Elmore Ranch fault

Table 4. Moment Comparison

Method	Moment ($x10^{25}$ dyne-cm)				Reference
	SH	ER	Total	Ratio	
GPS (Model 2)	9.4	2.3	11.7	4.1	This Study
Teleseismic	7.2	1.4	8.6	5.1	*Dziewonski et al.* [1988]
Teleseismic	10.	2.3	12.	4.3	*Sipkin* [1989]
Teleseismic	10.8	2.7	13.5	4.0	*Bent et al.* [1989]
Teleseismic	8.				*Hwang et al.* [1990]
Strong Motion	5.2				*Wald et al.* [1989]
Strong Motion	1.8				*Frankell and Wennerberg* [1989]
Pinyon Flat (Planar-A)	3.7	0.8	4.3	4.6	*Agnew and Wyatt* [1989]
EDM	9.3				*Lisowski and Savage* [1988]

SH - Superstition Hills fault
ER - Elmore Ranch fault

Figure Captions

Figure 1: Seismicity and major fault systems of the Imperial Valley. The Brawley Seismic Zone is the region of anomalously high activity between the northern Imperial and southern San Andreas faults. The valley represents a transition zone between crustal spreading in the Gulf of California to the south and right-lateral transform motion along the San Andreas system.

Figure 2: Seismicity and surface faulting associated with the November 24, 1987 Superstition Hills earthquake sequence. A M_S 6.2 event occurred along a northeast-trending structure (referred to here as the Elmore Ranch fault) and was followed by 12 hours with a M_S 6.6 event along the northwest-trending Superstition Hills fault. The focal mechanisms, aftershock distribution, and surface offset measurements are consistent with left-lateral strike-slip motion along the Elmore Ranch fault and right-lateral strike-slip motion along the Superstition Hills fault. A significant amount of postseismic slip was observed along the surface trace of the Superstition Hills fault, while activity essentially ceased on the Elmore Ranch fault after the M_S 6.6 event. The shaded strips along each fault indicate the geometrical extent of the dislocations used to model the geodetic displacements.

Figure 3: a) Imperial Valley and other GPS stations surveyed in 1986, 1988, and/or 1990. b) Central-southern Imperial Valley GPS stations surveyed in 1986, 1988, and/or 1990.

Figure 4: Imperial Valley GPS station displacements between 1986 and 1988. All movements are relative to station OCTI. The observed displacements are attributed to the 1987 earthquake sequence, secular plate-boundary deformation across the Imperial Valley, and measurement error. Movements near the 1987 rupture zone

approach 0.5 m. Error ellipses are determined by multiplying the formal errors by a variance factor, determined so the average error scales as 1 ppm (parts per million). The east-trending uncertainty is about 4 times larger than the north-trending uncertainty. The anomalous southwest-trending apparent movements for those stations to the southeast are attributed to measurement error.

Figure 5: Imperial Valley GPS station displacements between 1986 and 1990. The displacement at MOUN relative to BLAC is shown by the dashed arrow. For consistency with the 1986-1988 observations the estimated displacement at MOUN relative to OCTI is calculated by subtracting the estimated secular velocity of BLAC relative to OCTI obtained from conventional geodetic measurements (see Figure 9). Station MOUN was reset between surveys and site inspection during 1990 revealed a positioning error of about 15 cm.

Figure 6: Imperial Valley GPS station displacements between February/March 1988 and March/April 1988. The observed movements indicate the magnitude of errors due to the 1988 survey. The vector scale is twice that of Figures 4 and 5. The displacement at KANE could represent postseismic deformation from the 1987 earthquake sequence.

Figure 7: The best-fit solution to Model 1 (3-station inversion). The solid arrows indicate the observed displacements, while the dashed arrows represent the computed displacement based on Model 1. The shaded region indicates where horizontal displacements are greater than 4 cm.

Figure 8: The north and east-trending GPS displacement components for the 1986-1988 interval. All distances are computed relative to OCTI on a cross section trending N50°E, perpendicular to the plate motion direction. The effects of the

1987 Superstition Hills earthquake sequence based on Model 1 are removed. Open circles indicate stations where the seismic correction is greater than 4 cm (for that component). The 8.1 cm north-trending offset between stations on opposite sides of the valley is equivalent to 5.9 cm/yr displacement oriented N40°W. The large scatter for the east-trending component is presumably due to large measurement errors in the 1986 survey.

Figure 9: Imperial Valley EDM station velocities computed between 1972 and 1987 (solid arrows). The movements are largely attributed to secular deformation due to the relative motion between the North American and Pacific plates. The displacements are modeled (dashed arrows) by 3.45 cm/yr displacement across the valley, with right-lateral simple shear oriented N40°W occurring in a transition zones 50 km wide north of the Imperial Fault and 20 km wide to the south (shaded). The secular deformation is subtracted from the GPS displacements shown in Figures 4 and 5.

Figure 10: The residuals (observed minus calculated) for the best-fit solution to Model 2. The large residual components in the east-trending direction are suggestive of measurement error. The residual at MOUN is likely attributed to the reset benchmark between surveys. The unusually large discrepancy at L589 (and KANE) suggest additional seismic deformation not accounted for by the simple uniform slip parameterization considered for Model 2.

Figure 11: Observed surface slip along the Superstition Hills and Elmore Ranch faults (dashed lines). The Superstition Hills offsets were measured on January 25 and 26, 1988 about 1 month before the GPS observations. Decaying afterslip is recorded up to nearly 1 year after the earthquake sequence. The Elmore Ranch measurements are the cumulative slip from multiple surface breaks across a 10 km wide zone, with

no recorded postseismic offset after the earthquake. The discrete approximation to the surface slip used to constrain the uppermost sub-fault elements in Models 3a and 3b is shown by the solid lines.

Figure 12: The geodetic moment, standard deviation of sub-fault slip (instability), and solution RMS calculated for different singular values (k). a) Shown are solutions constrained by surface slip measurements ($20 \leq k \leq 30$). b) Shown are solutions unconstrained by surface slip measurements ($1 \leq k \leq 10$).

Figure 13: The horizontal slip distribution calculated independently for the Superstition Hills and Elmore Ranch faults based on Model 2. The shaded region indicates where the horizontal deformation is greater than 2 cm for the Superstition Hills fault and 0.5 cm for the Elmore Ranch fault. The scale for the Elmore Ranch event is altered to account for the smaller dislocation. The deformation pattern is almost identical between the two faults, although the displacement magnitudes are larger for the Superstition Hills event. This illustrates the difficulty in using the GPS measurements to resolve slip between the two faults.

Figure 14: Slip distribution along the Superstition Hills and Elmore Ranch faults computed from Singular Value Decomposition. Each fault is partitioned into the 50 sub-elements indicated by the grid spacing. a) Solutions for $k = 23$ and $k = 27$ constrained by measurements of surface offset. b) Solutions for $k = 3$ and $k = 7$ unconstrained by surface slip measurements.

Figure 15: Known and/or potential conjugate/cross-fault seismic episodes in the Imperial Valley since 1900. Seismic release on (left-lateral) northeast-trending structures was observed in 1979, 1981, and 1987. Earthquake pairs or mainshock/aftershock sequences suggestive of conjugate faulting were observed in

1915, 1927, 1940. This suggests conjugate/cross-fault interaction is typical for the Imperial Valley.

Figure 16: Strike-shear (right-lateral positive) and normal stress change (dilatation positive) induced on the Superstition Hills fault due to a 30 cm left-lateral Elmore Ranch dislocation (Model 2). Also shown is the Coulomb failure stress change, where positive values indicate an increased potential for rupture (earthquake inducing stress). The northwest third of the 1987 Superstition Hills rupture plane underwent a stress change tending it toward failure with the maximum change calculated in the epicentral region near the intersection with the Elmore Ranch fault. There was no rupture to the northwest where the Coulomb failure stress was negative (reduced earthquake potential). The magnitude of the stress change (in bars) is in the range of typical earthquake stress drops.

Figure 17: Schematic of potential earthquake failure processes in the Imperial Valley. a) Earthquake failure occurs after some critical stress is reached. b) Earthquake failure occurs following a time dependent delay after critical stress is exceeded.

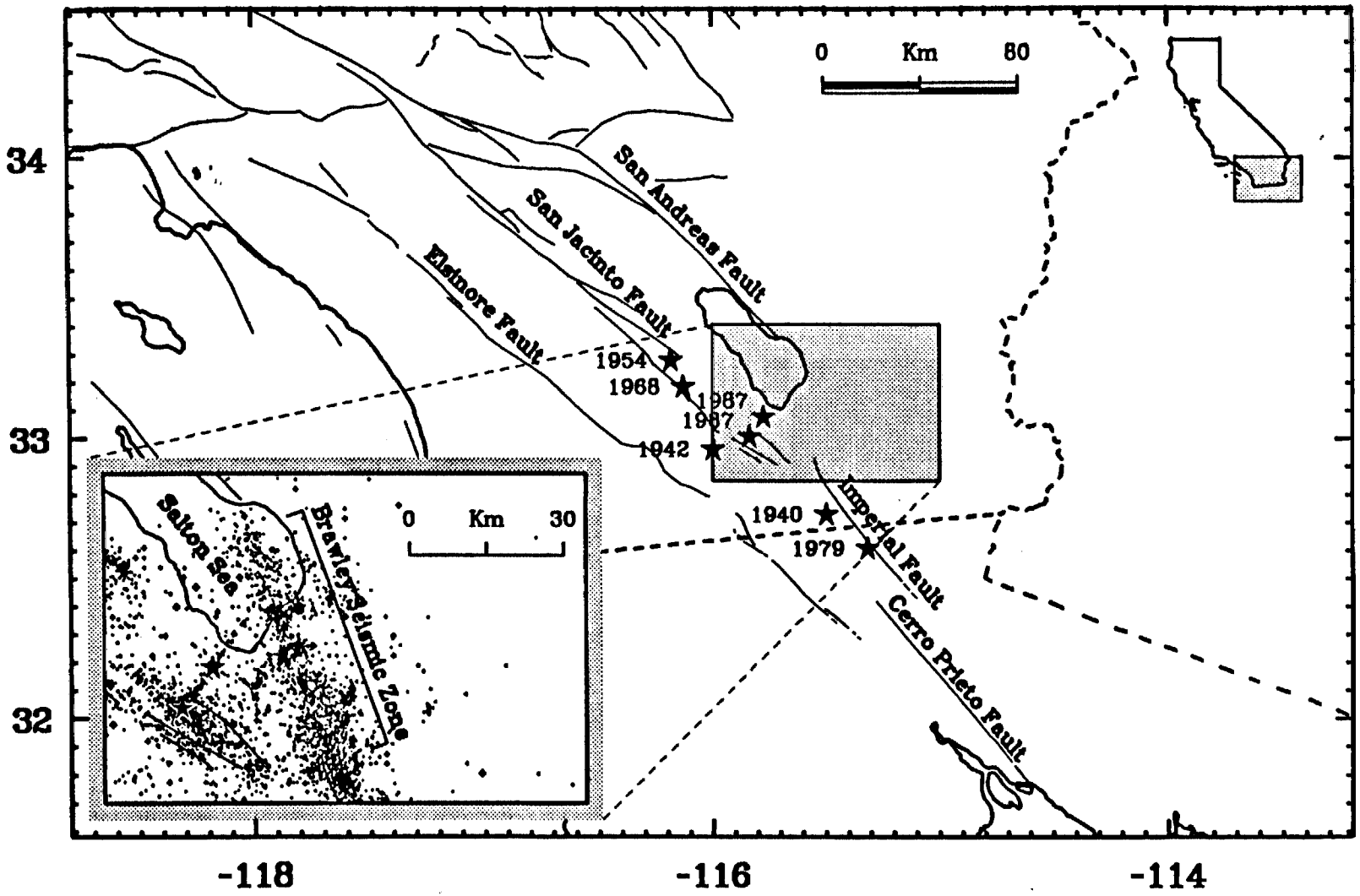
0 Km 80
San Andreas Fault
San Jacinto Fault
Elsinore Fault
1954
1968
1987
1987
1942
1940
1979
Imperial Fault
Cerro Prieto Fault
0 Km 30
Salton Sea
Brawley Seismic Zone
34
33
32
-118
-116
-114

Figure 1

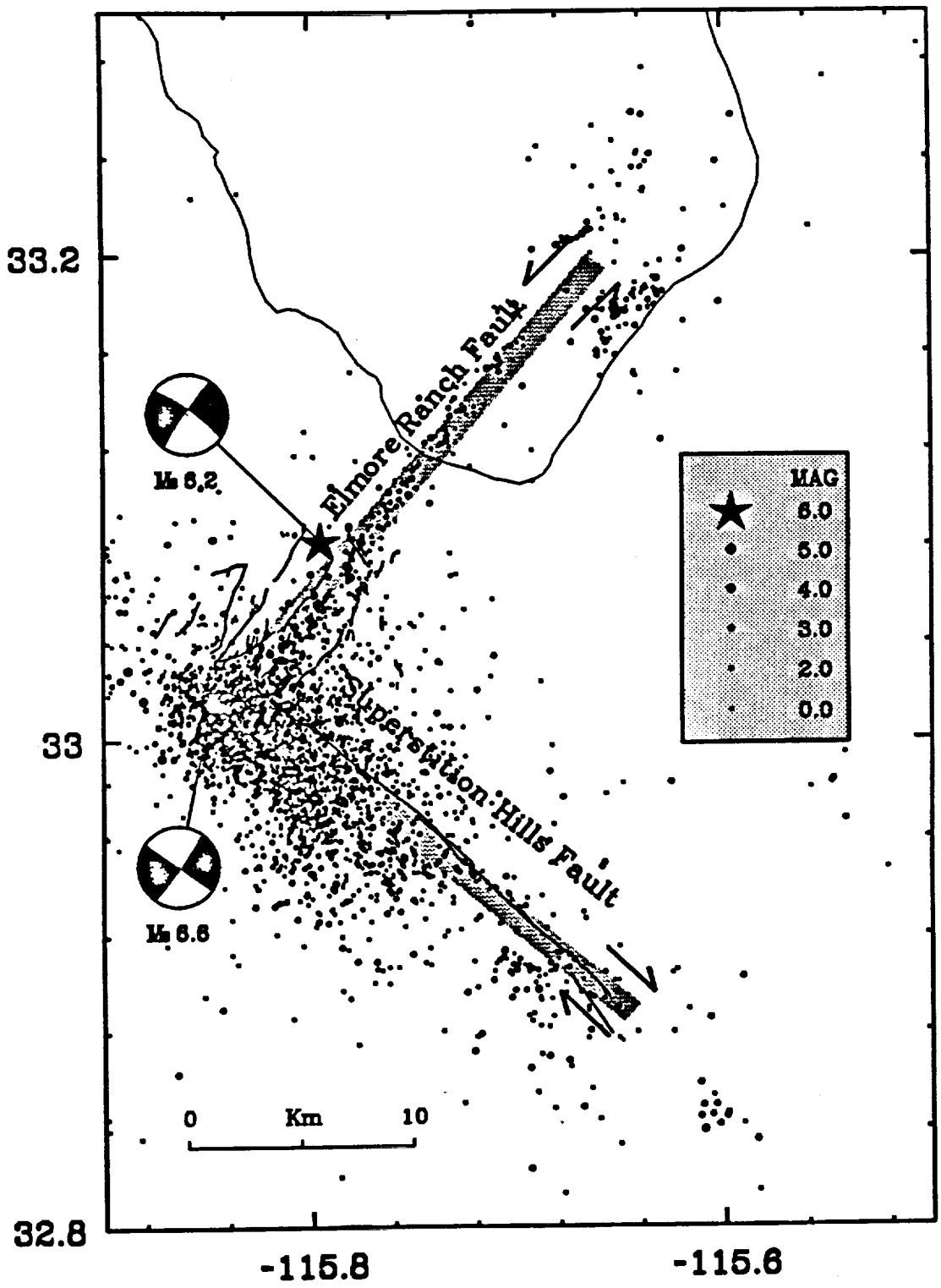
33.2
33
32.8
-115.8
-115.6
Elmore Ranch Fault
Superstition Hills Fault
Ms 6.2
Ms 6.6
MAG
6.0
5.0
4.0
3.0
2.0
0.0
0
Km
10

Figure 2

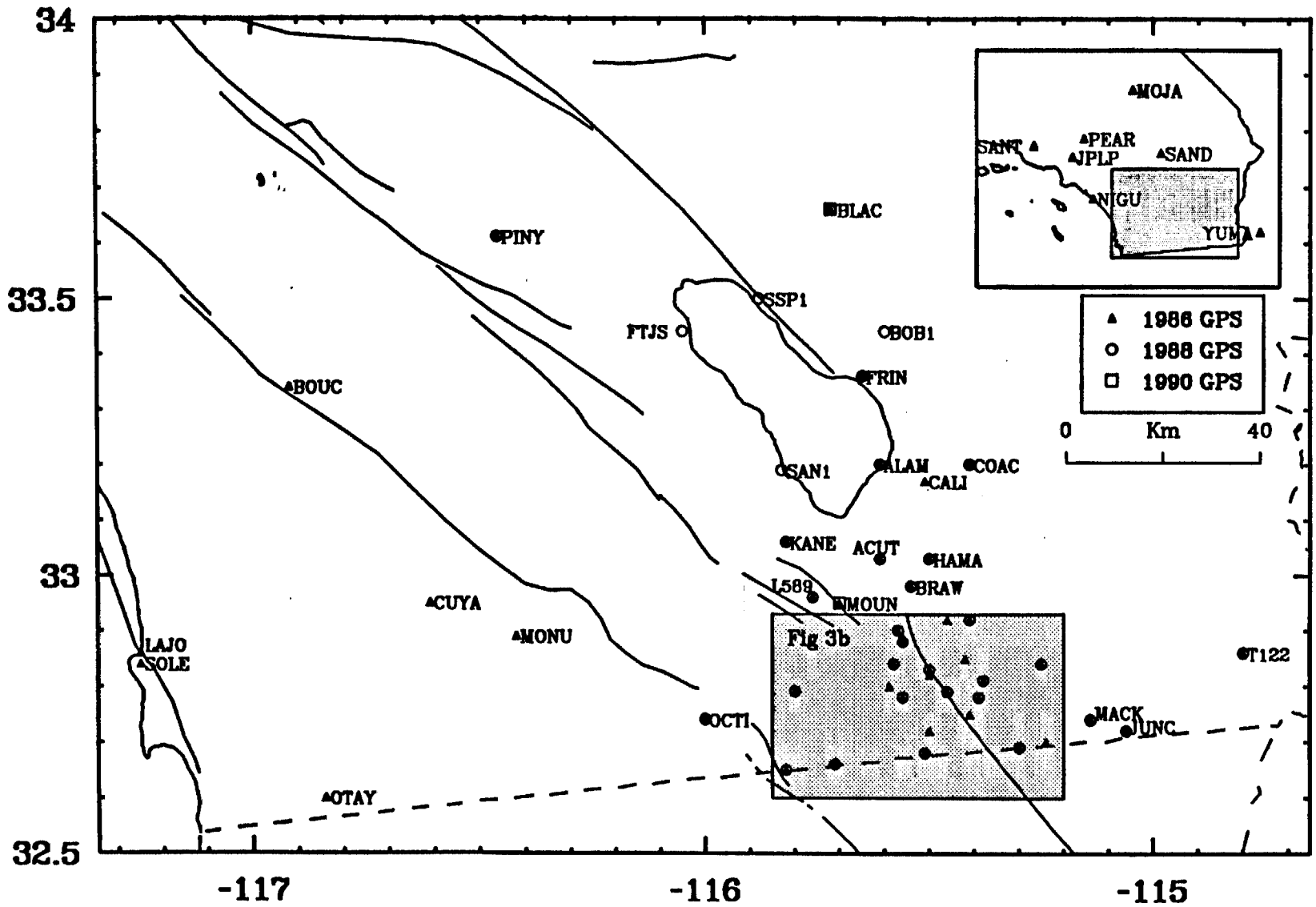
34
33.5
33
32.5
-117
-116
-115
MOJA
PEAR
SAND
JPLP
SANT
NIGU
YUMA
1986 GPS
1988 GPS
1990 GPS
0
Km
40
BLAC
PINY
SSP1
FTJS
BOB1
FRIN
BOUC
SAN1
ALAM
COAC
CALI
KANE
ACUT
HAMA
BRAW
L589
MOUN
CUYA
MONU
LAJO
SOLE
Fig 3b
T122
OCTI
MACK
UNC
OTAY

Figure 3a

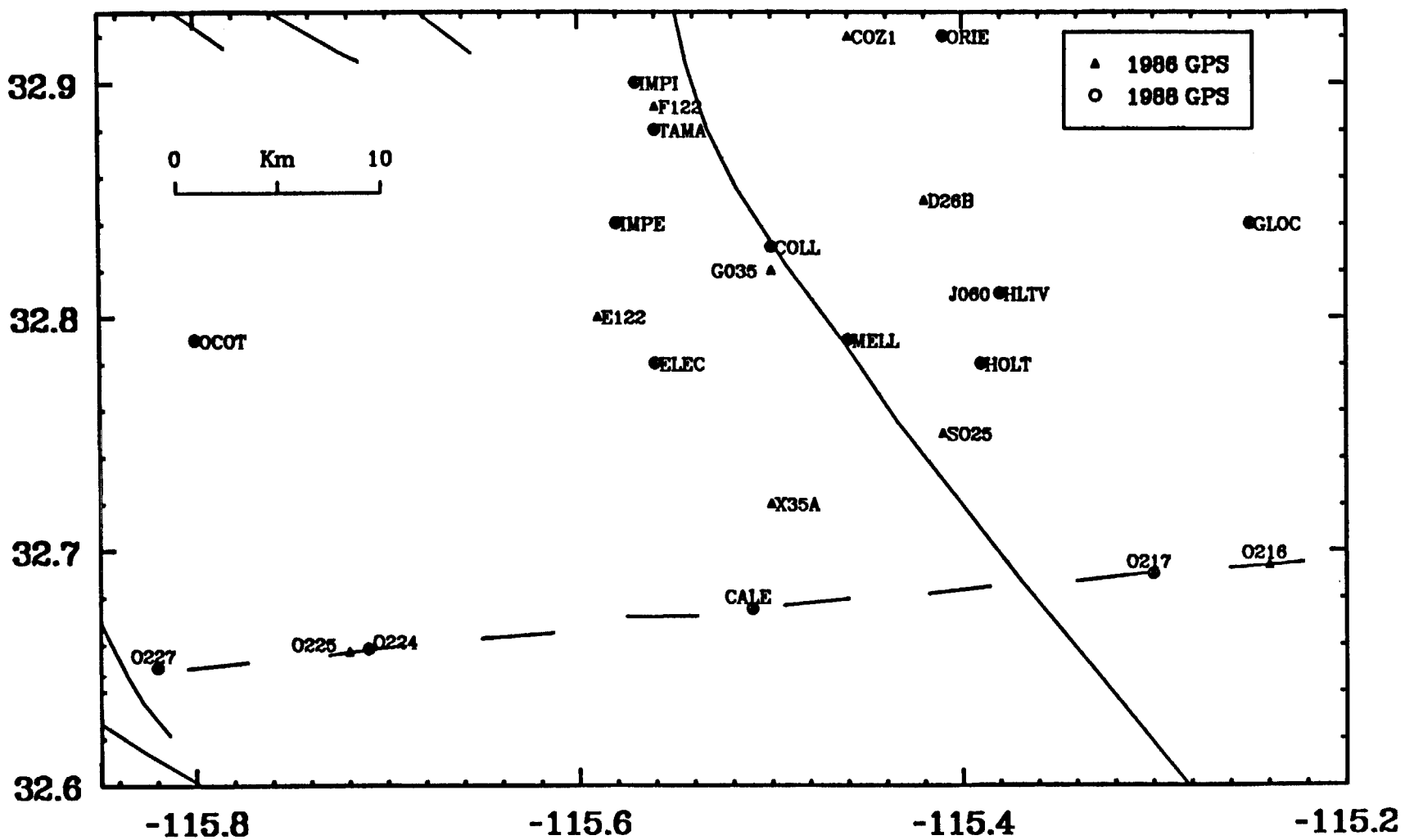
1986 GPS
1988 GPS
0 Km 10
COZ1
ORIE
IMPI
F122
TAMA
D26B
GLOC
IMPE
COLL
G035
J060
HLTV
E122
MELL
OCOT
ELEC
HOLT
SO25
X35A
0217
0216
CALE
0227
0225
0224
32.9
32.8
32.7
32.6
-115.8
-115.6
-115.4
-115.2

Figure 3b

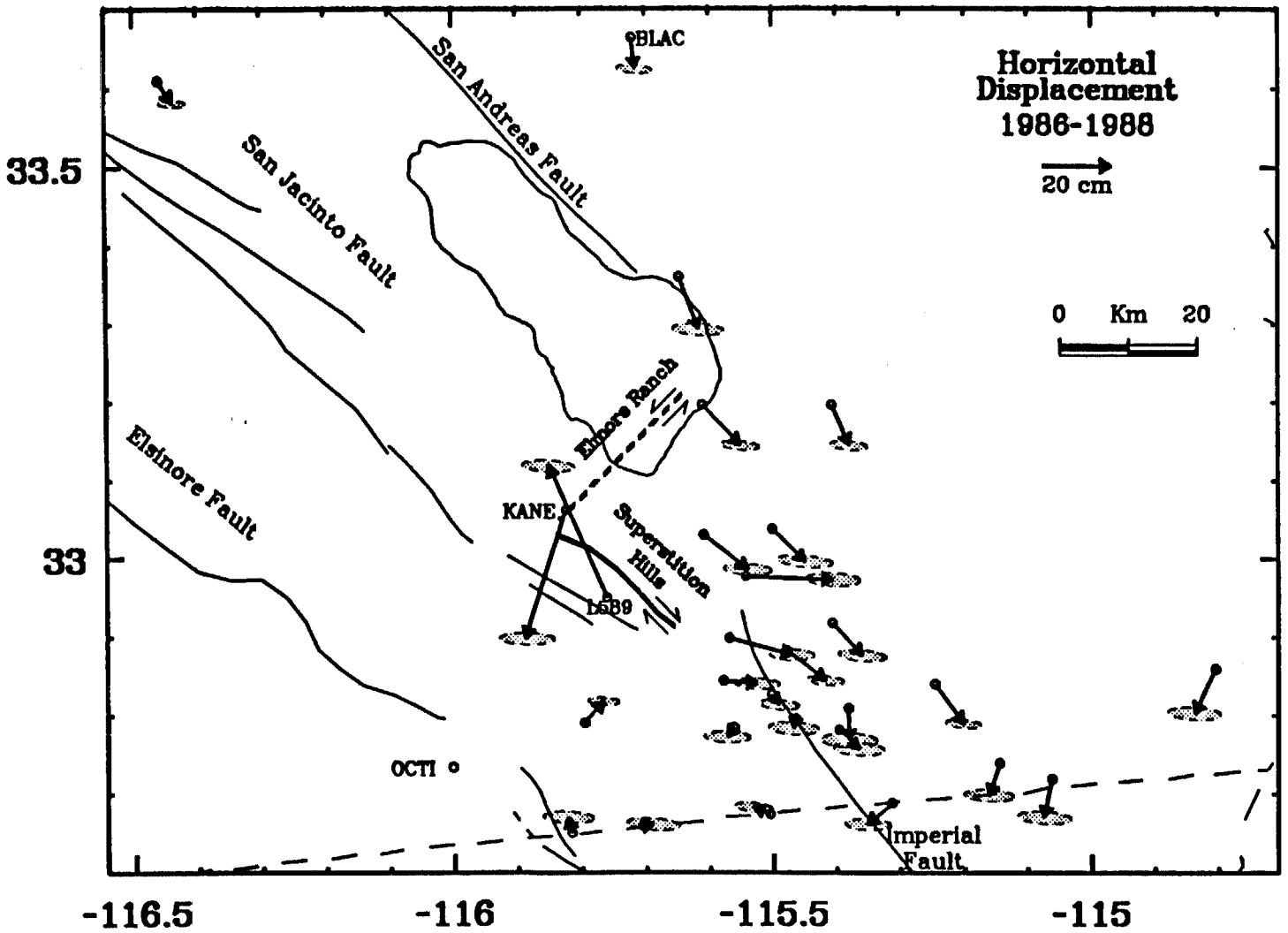
Horizontal
Displacement
1986-1988
20 cm
0 Km 20
BLAC
San Andreas Fault
San Jacinto Fault
Elsinore Fault
Elmore Ranch
KANE
Superstition
Hills
B589
OCTI
Imperial
Fault
33.5
33
-116.5
-116
-115.5
-115

Figure 4

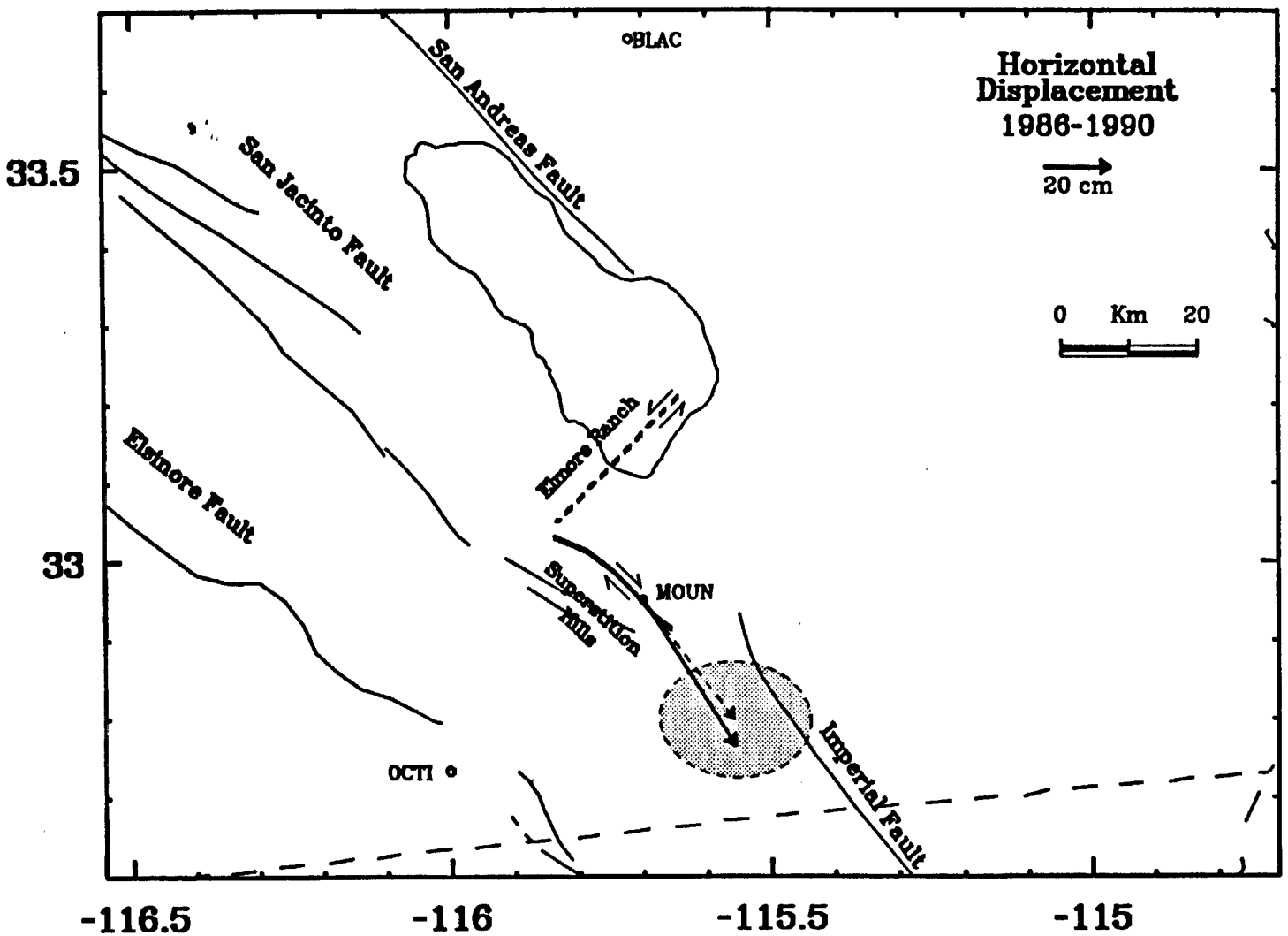
Horizontal
Displacement
1986-1990
20 cm
0 Km 20
BLAC
San Andreas Fault
San Jacinto Fault
Elsinore Fault
Elmore Ranch
Superstition
Hills
MOUN
OCTI
Imperial Fault
33.5
33
-116.5
-116
-115.5
-115

Figure 5

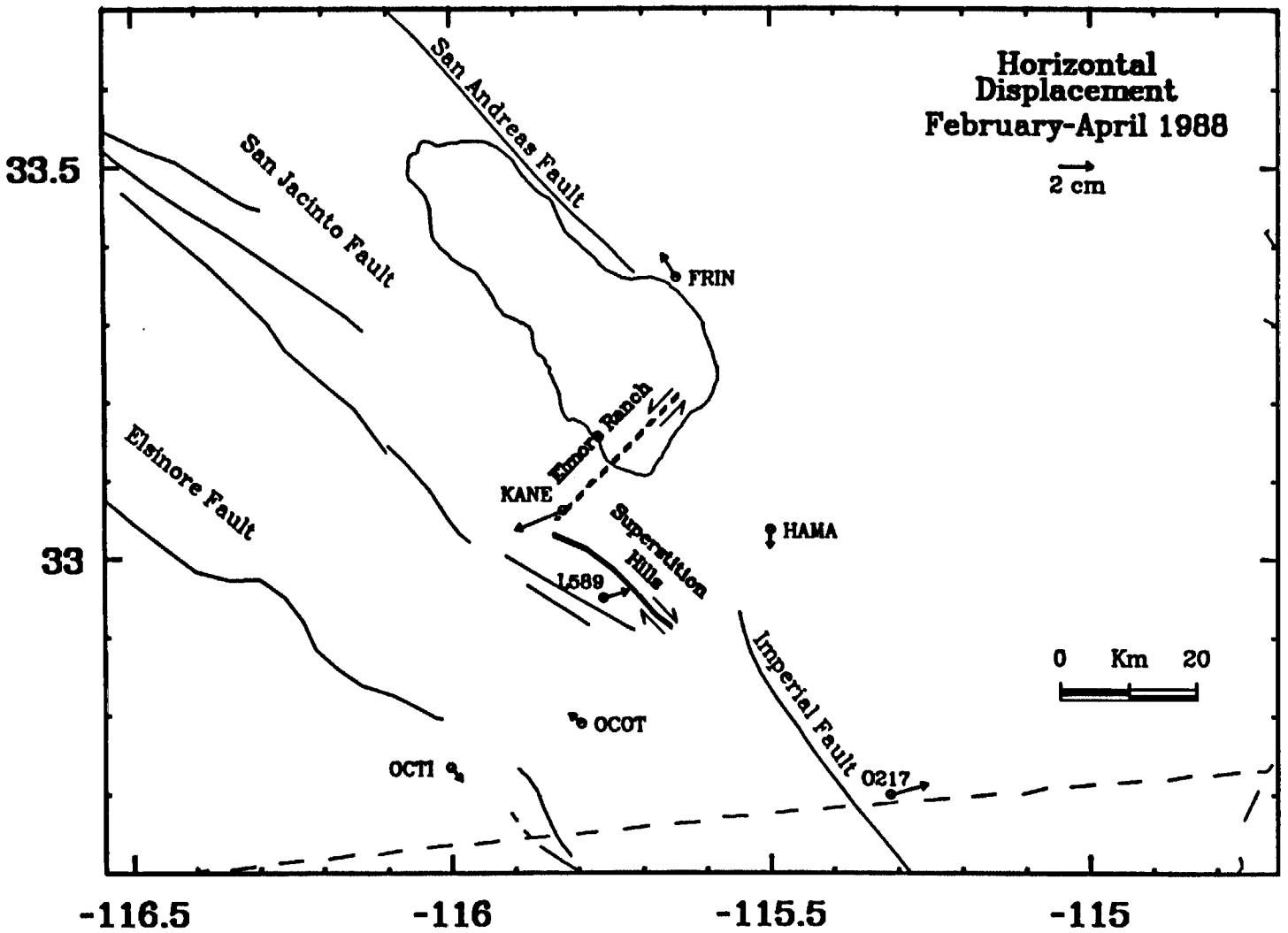
Horizontal
Displacement
February-April 1988
2 cm
San Andreas Fault
San Jacinto Fault
Elsinore Fault
Imperial Fault
FRIN
Elmore Ranch
KANE
Superstition
Hills
HAMA
1589
OCOT
OCTI
0217
0 Km 20
33.5
33
-116.5
-116
-115.5
-115

Figure 6

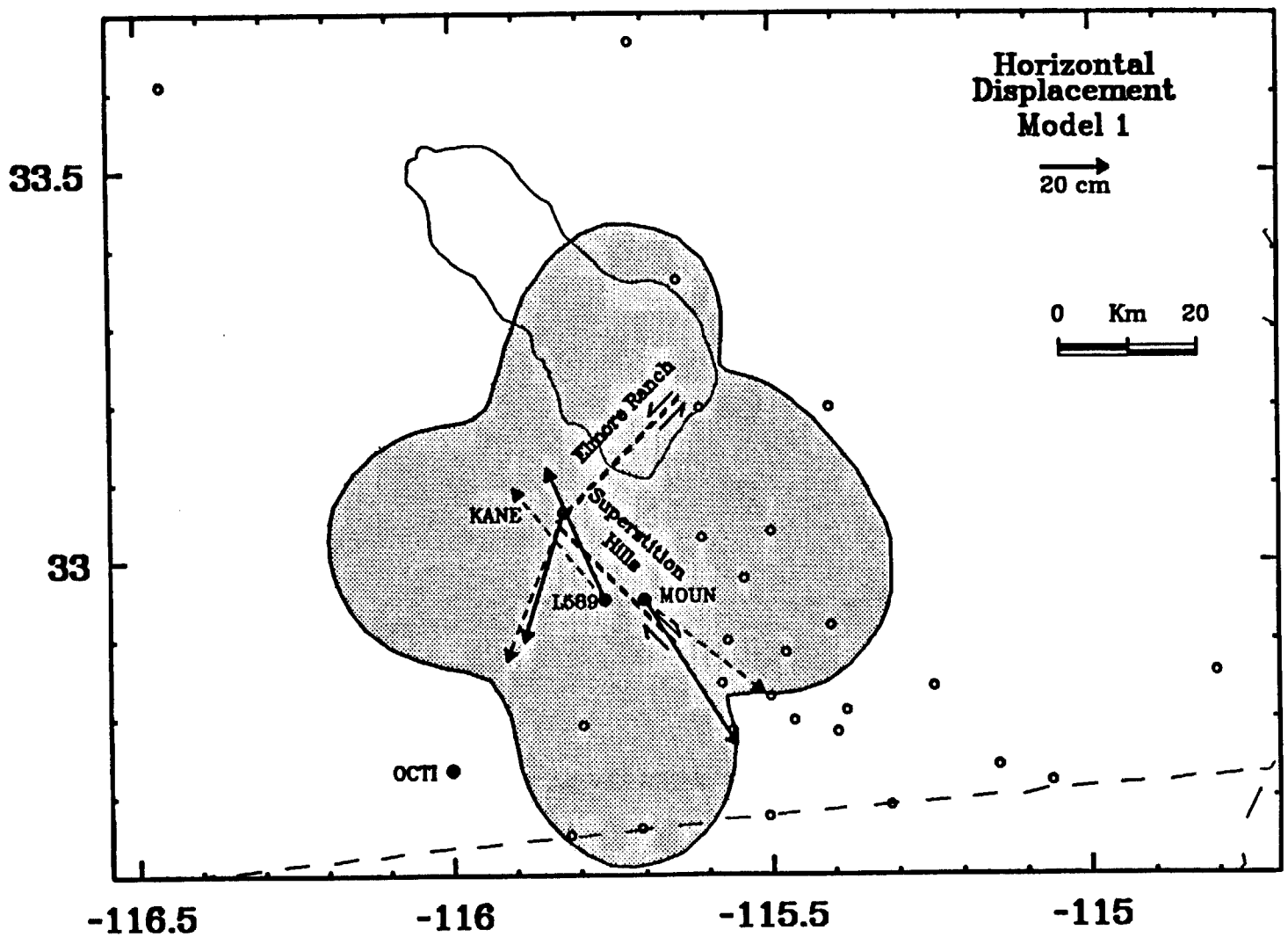
Horizontal
Displacement
Model 1
20 cm
0 Km 20
33.5
33
-116.5
-116
-115.5
-115
Elmore Ranch
Superstition
Hills
KANE
I569
MOUN
OCTI

Figure 7

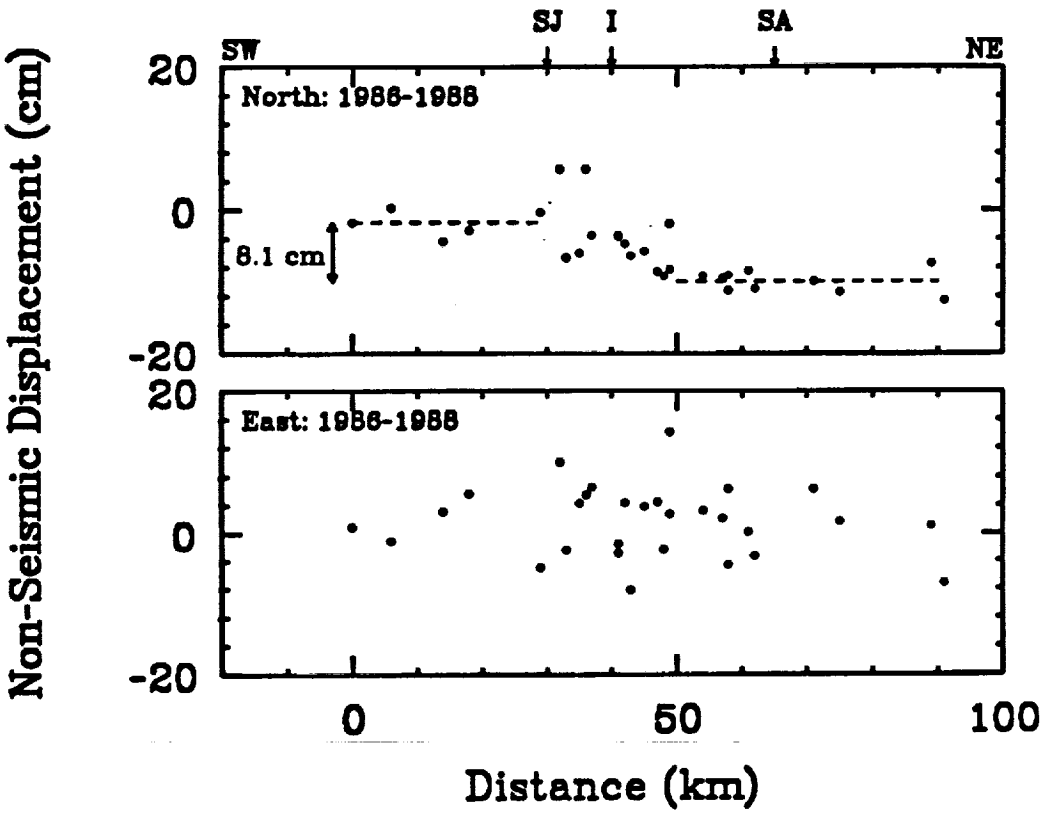
SJ
I
SA
SW
NE
20
0
-20
North: 1986-1988
8.1 cm
East: 1986-1988
0
50
100
Non-Seismic Displacement (cm)
Distance (km)

Figure 8

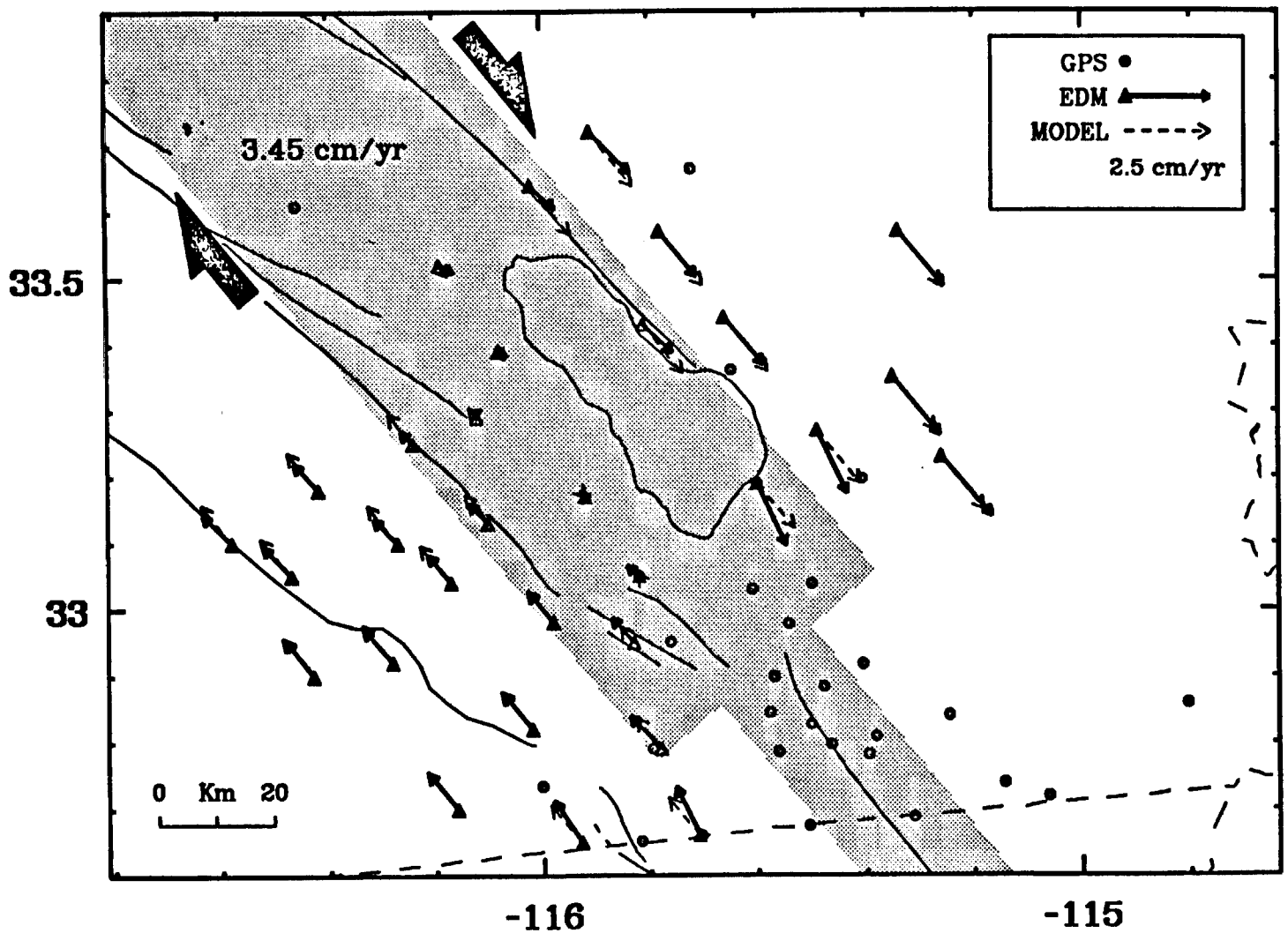

Figure 9

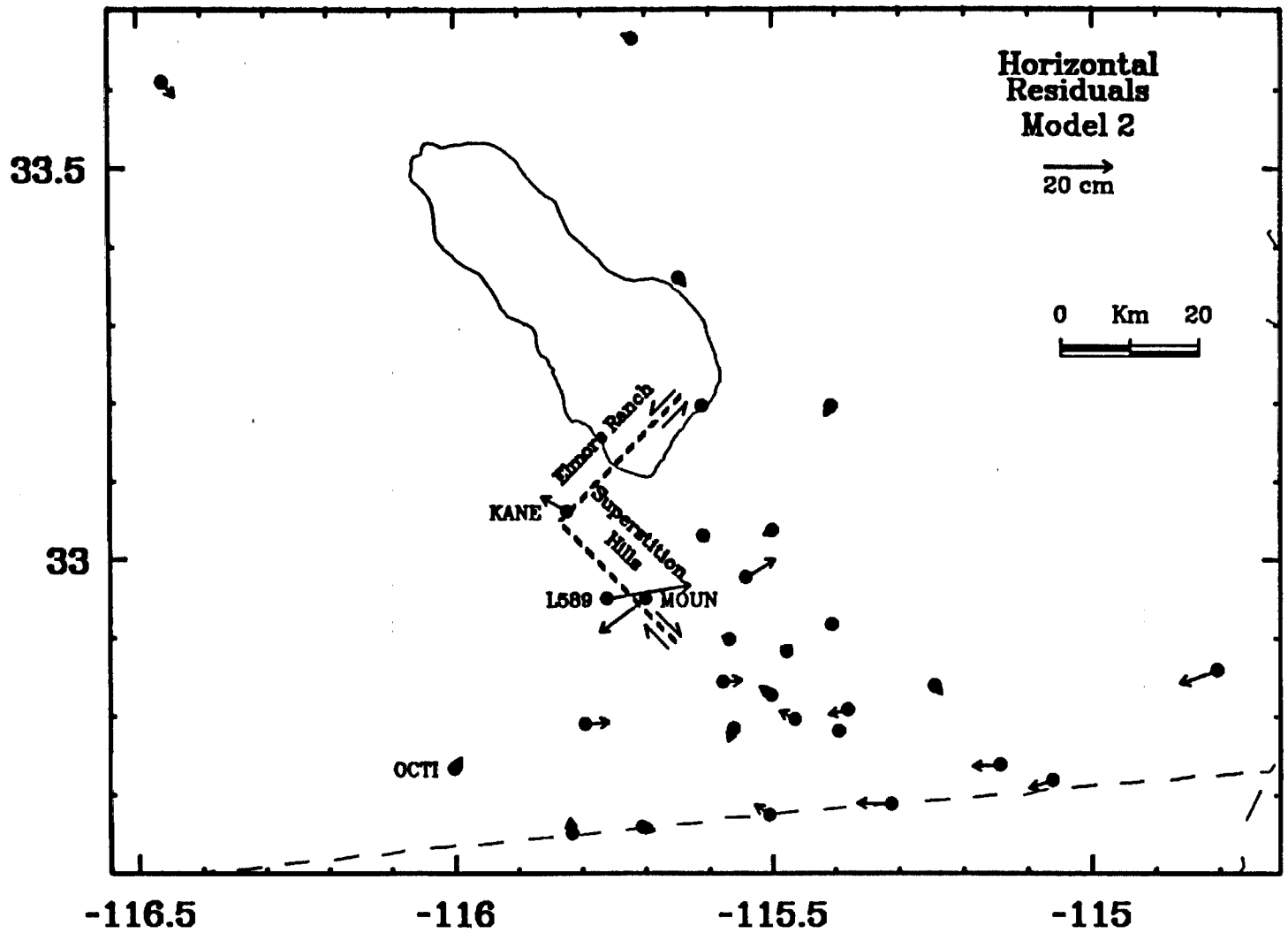
Horizontal
Residuals
Model 2
20 cm
0 Km 20
33.5
33
-116.5
-116
-115.5
-115
Emory Ranch
KANE
Superstition
Hills
L589
MOUN
OCTI

Figure 10

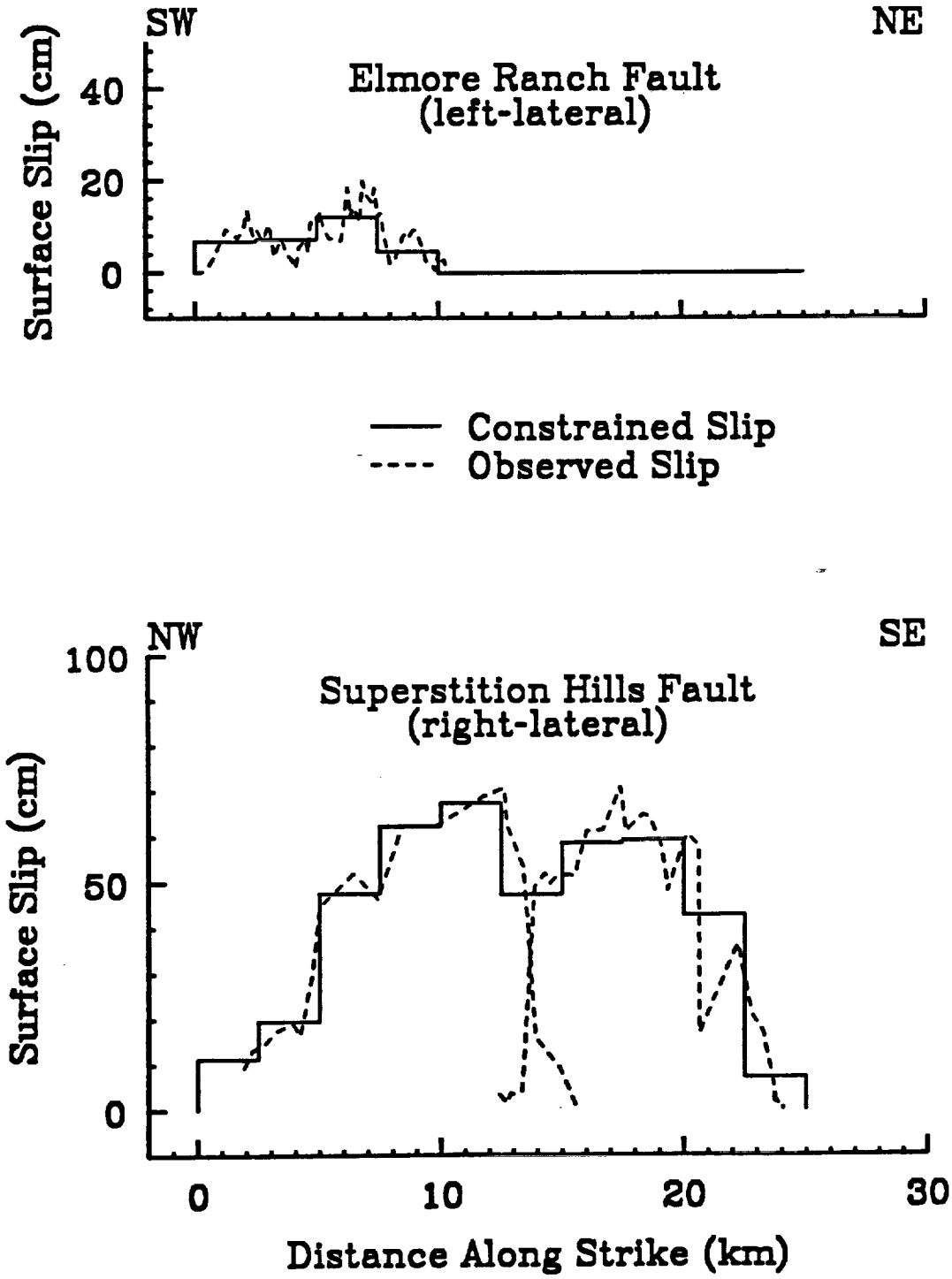
SW
NE
Elmore Ranch Fault
(left-lateral)
Surface Slip (cm)
40
20
0
Constrained Slip
Observed Slip
NW
SE
Superstition Hills Fault
(right-lateral)
Surface Slip (cm)
100
50
0
0
10
20
30
Distance Along Strike (km)

Figure 11

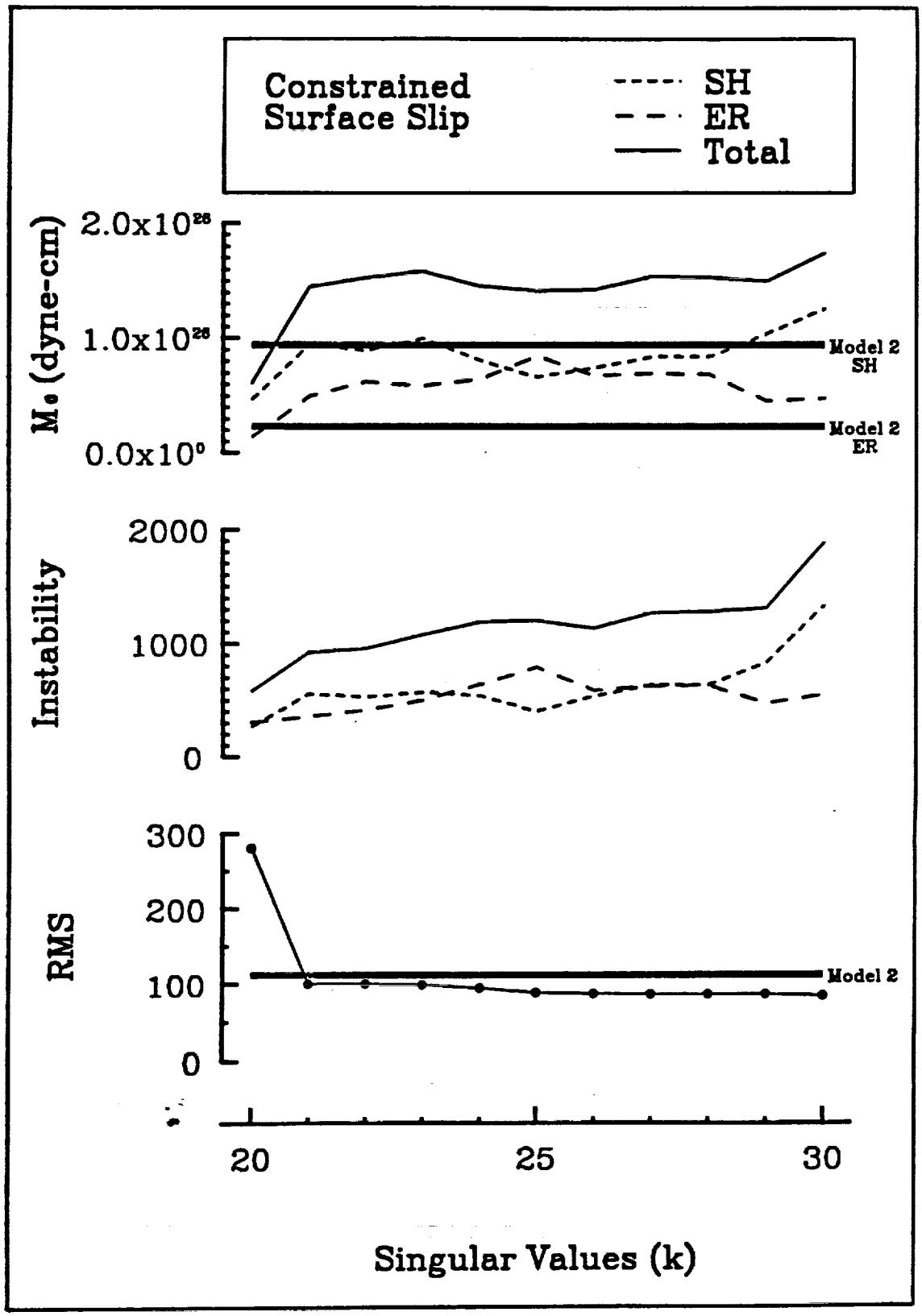
Constrained
Surface Slip
SH
ER
Total
M_o (dyne-cm)
2.0x10²⁶
1.0x10²⁶
0.0x10⁰
Model 2
SH
Model 2
ER
Instability
2000
1000
0
RMS
300
200
100
0
Model 2
20
25
30
Singular Values (k)

Figure 12a

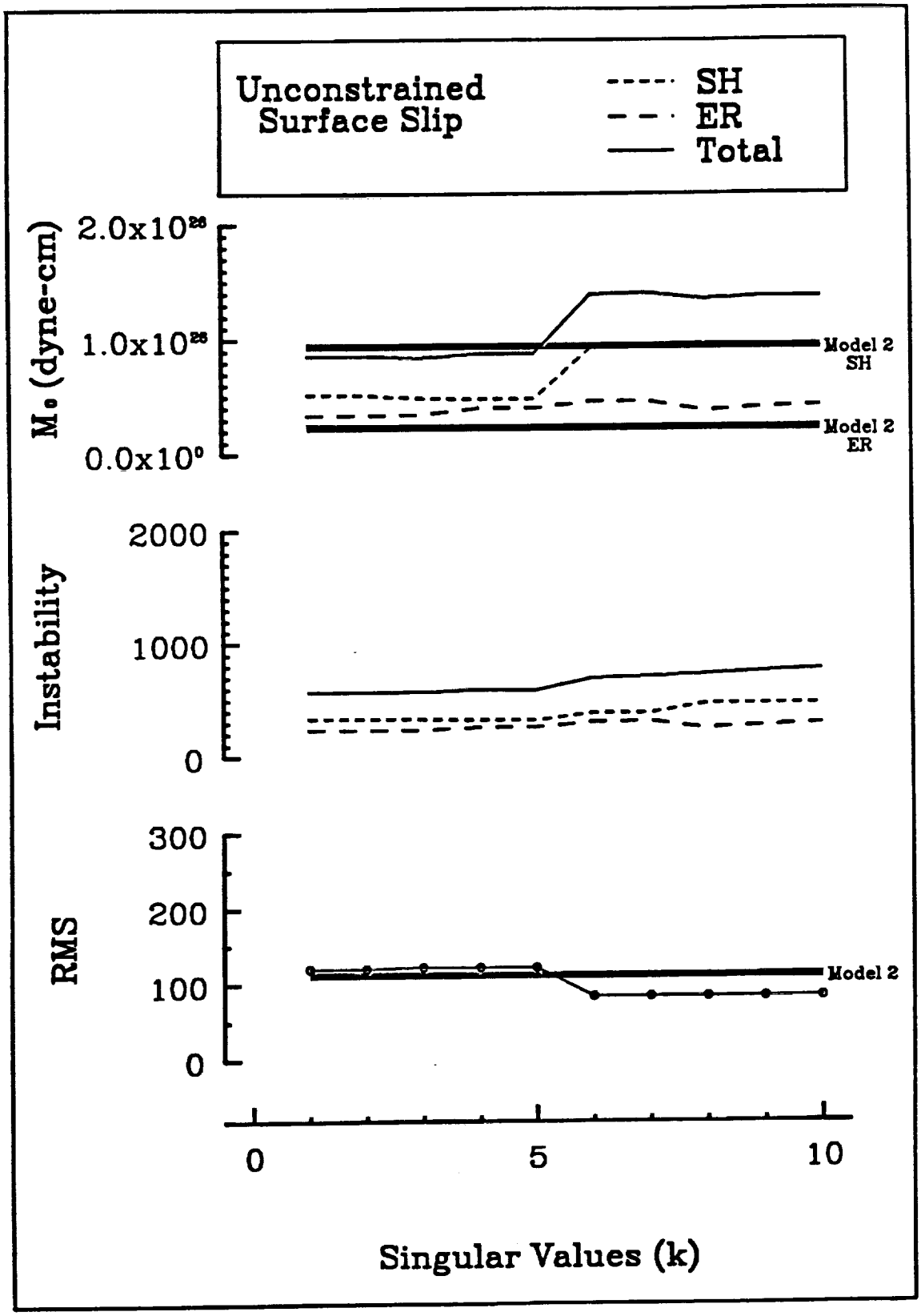
Unconstrained
Surface Slip
SH
ER
Total
2.0x10²⁶
1.0x10²⁶
0.0x10⁰
Mₒ (dyne-cm)
Model 2
SH
Model 2
ER
2000
1000
0
Instability
300
200
100
0
RMS
Model 2
0
5
10
Singular Values (k)

Figure 12b

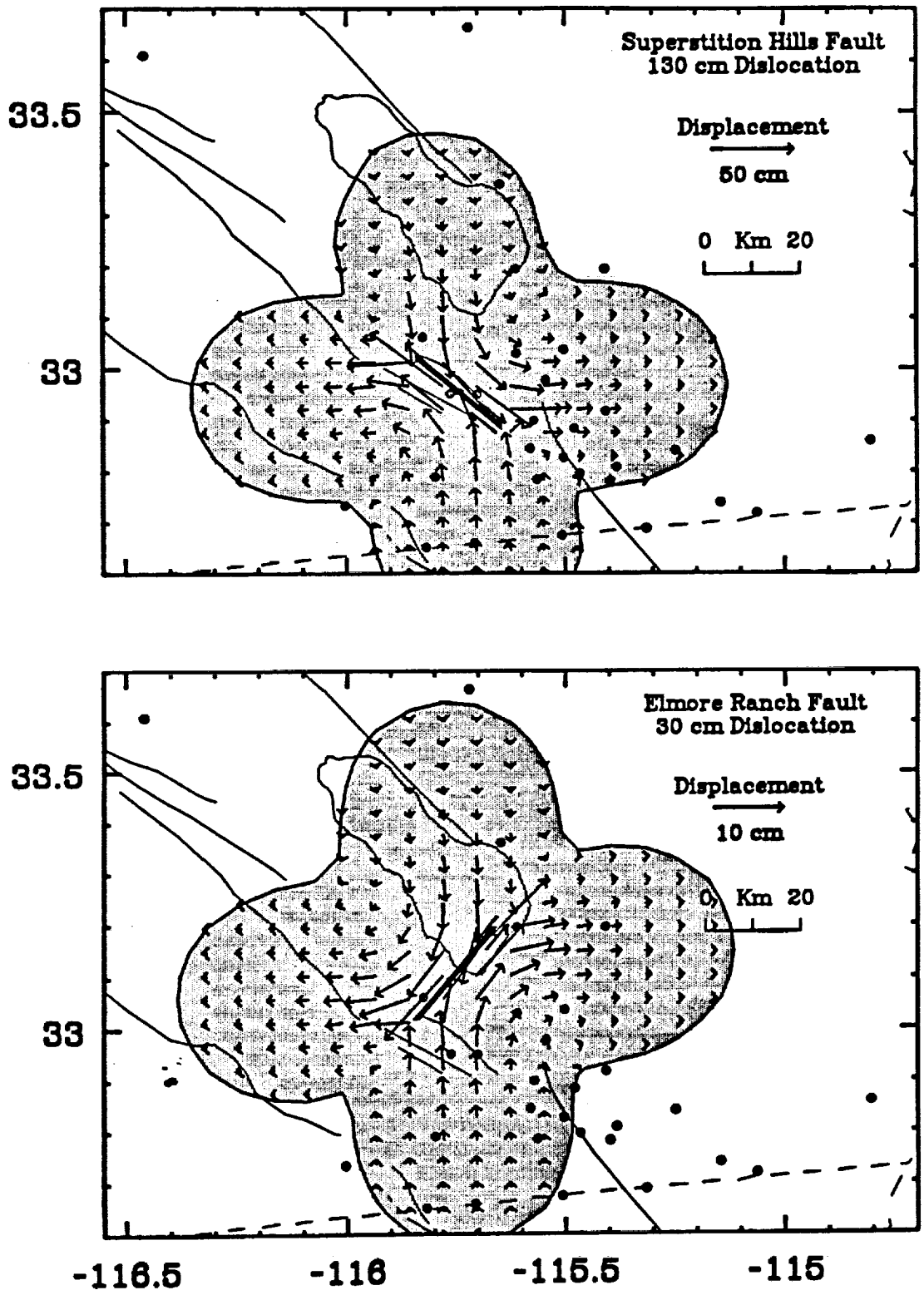
Superstition Hills Fault
130 cm Dislocation
Displacement
50 cm
0 Km 20
33.5
33
Elmore Ranch Fault
30 cm Dislocation
Displacement
10 cm
0 Km 20
33.5
33
-116.5
-116
-115.5
-115

Figure 13